Cement and Concrete Research 164 (2023) 107062

Contents lists available at ScienceDirect

Cement and Concrete Research

journal homepage: www.elsevier.com/locate/cemconres

Nanosized belite phases obtained by flame spray pyrolysis: Assessment of process conditions on the mineralogy and reactivity

Natalia Betancur-Granados [a,c,*], Herbert Pöllmann [b], Oscar Jaime Restrepo-Baena [c], Jorge I. Tobón [c]

[a] Facultad de Ingeniería, Grupo Innovación e Ingeniería I^2, Corporación Universitaria Minuto de Dios - UNIMINUTO, Cra. 45 No. 22D - 25 - Km 0 Autopista Medellín - Bogotá, 051052 Bello, Colombia

[b] Institute of Geosciences and Geography, Mineralogy/Geochemistry, University of Halle, Von-Seckendorff-Platz 3, 06120 Halle, Germany

[c] Grupo del Cemento y Materiales de Construcción (CEMATCO), Materials and Minerals Department, Universidad Nacional de Colombia, Colombia

ARTICLE INFO

Keywords:
Belite
Dicalcium silicate
Flame spray pyrolysis
Process conditions
Mineralogy
Reactivity

ABSTRACT

The synthesis of highly reactive dicalcium silicate phases by the alternative method flame spray pyrolysis (FSP) was investigated. Five main conditions of the synthesis process were varied and analyzed by applying a two-level fractional factorial design 2^{5-2} resolution III, with a replica of a chemical system defined by a mixture of Ca $(O_2CCH_2CH_3)_2$/Si$(C_2H_5O))_4$ dissolved in ethanol/water/triethanolamine to evaluate the formation of polymorphs and their reactivity. For this, a physical and mineralogical characterization was carried out that included X-ray diffraction (XRD), Fourier transform infrared spectroscopy (FT-IR), Brunauer-Emmett-Teller (BET) specific surface area analysis, thermogravimetric analysis (TGA-DSC), and transmission electron microscopy (TEM). The investigation reveals that the process parameters have a remarkable importance on the final properties of the samples, favoring the formation of belite phases with high reproducibility. The hydraulic samples present a complete hydration reaction after 24 h of contact with water, giving a clear image of the potential of this technique for the development of highly reactive materials that can be part of sustainable construction in the future.

1. Introduction

The production of nanoparticles by emerging methods allows the synthesis of materials with high performance in processes with less negative impact on the environment [1,2]. In the cement industry, the production of dicalcium silicates (Ca_2SiO_4) at the nanometric level allows the formation of highly reactive materials with cementitious properties, which are used in civil structures applications and the development of bioceramics for medical applications [3–5].

The main component of commercial portland cement (PC) is tricalcium silicate (alite), which together with dicalcium silicate (belite), give cement its mechanical properties, so that, Ca_3SiO_5 develops compressive strength at early ages (1 month) and Ca_2SiO_4 at late ages (1 year) due to its slow reactivity [6,7]. Alternative cements that have dicalcium silicate (Ca_2SiO_4) as their main component have some advantages such as a lower energy and calcium oxide material demand than tricalcium silicate and lower carbon dioxide emissions during the decomposition of calcite [8,9]. However, among its disadvantages are the low reactivity and the high hardness of the material for subsequent grinding. Increasing the reactivity of dicalcium silicate through its production as nanoparticles would minimize its disadvantages associated with reactivity, reducing the negative impact on the environment due to the lower calcium consumption of belite [9–11].

For this, alternative mass production process, as aerosol methods, that allow the continuous production of nanosized Ca_2SiO_4 are sought [12]. However, there is a lot of additional research to be done in the production of materials with a high number of polymorphism such as Ca_2SiO_4 synthesized by these techniques, in which each of the polymorphs plays an important role in the reactivity of the material due to the arrangement of the SiO^{+4} tetrahedra and Ca^{2+} ions, and their formation conditions [11].

Considering the above, flame spray pyrolysis (FSP) is a highly efficient continuous method for the formation of nanoparticles, postulated as one of the most viable production processes with high production

* Corresponding author at: Facultad de Ingeniería, Grupo Innovación e Ingeniería I^2, Corporación Universitaria Minuto de Dios - UNIMINUTO, Cra. 45 No. 22D - 25 - Km 0 Autopista Medellín - Bogotá, 051052 Bello, Colombia.
E-mail address: natalia.betancur.g@uniminuto.edu.co (N. Betancur-Granados).

https://doi.org/10.1016/j.cemconres.2022.107062
Received 17 May 2022; Received in revised form 10 October 2022; Accepted 1 December 2022
Available online 6 December 2022

Table 1
Preparation of the starting solution.

Solvent mixtures		Ceramic loading	
		2.5 %	5 %
Solvent 1	Ethanol (mL) (0.7)	710	355
	Water (mL) (0.25)	200	100
	Methanol (mL) (0.05)	51	25.5
Solvent 2	Ethanol (mL) (0.75)	200	100
	Water (mL) (0.25)	760	380

scale and low environmental impact than other processes [13,14]. Therefore, for the successful production of belite phases, it is necessary to understand the effect of process conditions on characteristics such as mineralogy and reactivity, due to the complexity of the system that can be affected by the combustion environment of this process.

Therefore, in this research nanosized belite phases of cement were synthesized by flame spray pyrolysis (FSP) using a statistical design, evaluating the formation of polymorphs and their stability by varying the process parameters during the synthesis. The products were characterized physically and mineralogically using X-ray diffraction (XRD), Fourier-transform infrared spectroscopy (FT-IR), Brunauer-Emmett-Teller (BET) specific surface area, thermogravimetric analysis (TGA-DSC), and transmission electron microscopy (TEM) as a first step to understand the material to evaluate its potential for use in cementitious applications or the identification of other applications. It was possible to identify process parameters that favor the formation of highly reactive belite phases, giving a clearer picture of the potential for using this technique for the development of highly reactive materials that can be part of the sustainable construction in the future.

2. Material and methods

2.1. Starting solution

During the synthesis processes, tetraethyl orthosilicate (TEOS) ($Si(OC_2H_5)_4$, 99 %) from Sigma Aldrich, calcium propionate ($(C_2H_5COO)_2$, 98 %) from Protokimika S.A, triethanolamine (TEA) pure, pharma grade from PanReac AppliChem were used as precursors for the starting solution, while ethanol from Protokimica (96 %), methanol from Sigma-Aldrich (99.8 %) and deionized water where used as solvents during the reaction processes.

The chemical system was defined by a mixture of $Ca(O_2CCH_2CH_3)_2$/$Si(C_2H_5O)_4$ dissolved in ethanol/water/TEA [15]. The starting solution to obtain 6 g of product, considering an equipment yield of 30 %, was prepared by dissolving calcium propionate, $Ca(O_2CCH_2CH_3)_2$, 98 % (44.1287 g, 0.2369 mol), in 200 mL of distilled water in 1 L beaker. Tetraethyl orthosilicate, $Si(C_2H_5O)_4$, 99 % (24.4353 g, 0.1172 mol) was dissolved in 200 mL of ethanol and added slowly to the calcium propionate solution. Then, triethanolamine, $C_6H_{15}NO_3$, 98 % was added dropwise to avoid the formation of emulsions in the starting solution (3.5 mL, 0.0263 mol are added to ceramic loadings of 5 % and 7 mL, 0.0527 mol are added to ceramic loadings of 2.5 %). The solvent mixture was prepared considering the solvent and the ceramic loading (chemical system) as shown in Table 1. The solution was stirred for 10 min and then, it was brought to the synthesis equipment.

2.2. Synthesis method

After preparing the starting solution, the synthesis procedure (Fig. 1) consists in lighting and adjusting the oxy-acetylene torches to a slightly oxidizing flame (Acetylene flow: 0.011 m^3/min, Oxygen flow: 0.019 m^3/min). Then, the cooling system and the electrostatic precipitator must be light-up. Once the equipment is turned on, the solution is pumped using a dispensing peristaltic pump, model NE-9000G, and aerosolized with an airblast nozzle through the flames, using the levels of process parameters defined during the design of experiments. This results in the evaporation/reaction of the precursors in the flame and subsequent formation of the ceramic particles.

Droplet uniformity during the spraying process and droplet size are important factors in describing spray quality. Droplet sizes are calculated using the Sauter Mean Diameter (SMD) Eq. (1) for plain-jet airblast atomizers described by Nukiyama & Tanasaw, which is considered the most appropriate equation in aerosol processes with mass and heat

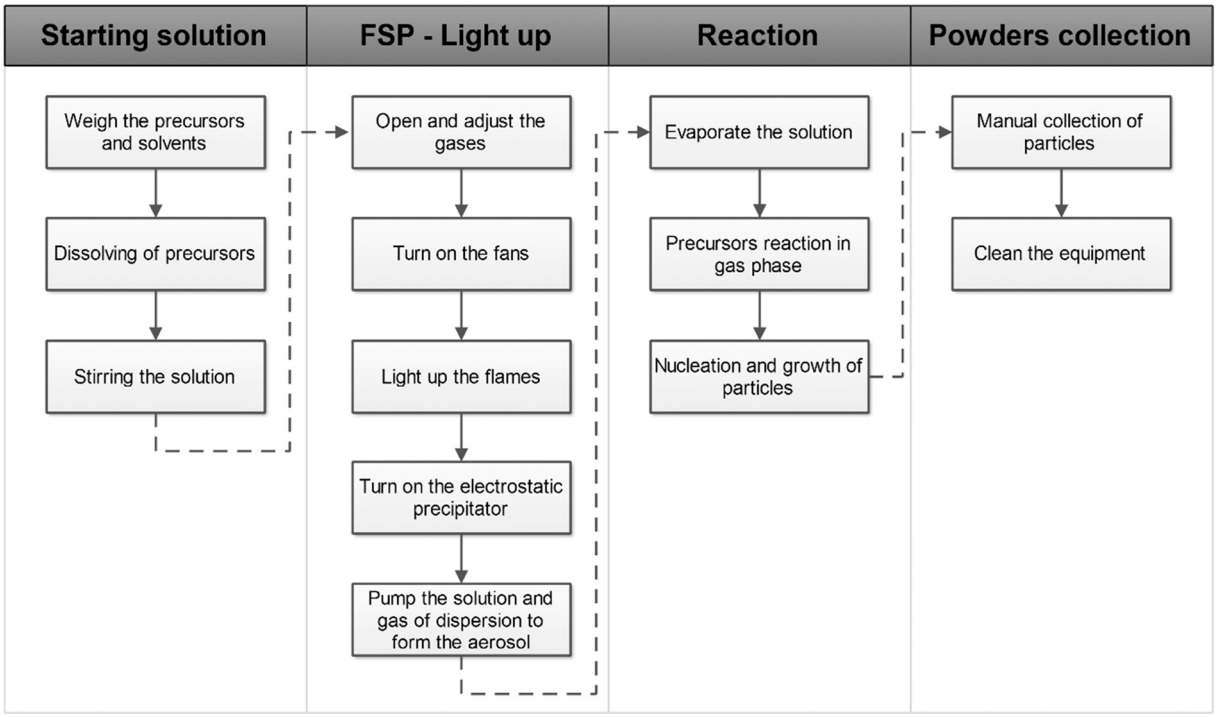

Fig. 1. General FSP synthesis procedure.

Table 2
Sauter Mean Diameter (SMD)and air/liquid mass ratio (ALR) values at different process conditions.

Flow rate (mL/min)-dispersion pressure (kPa)	SMD (mm)	ALR ($D_{1.1}$)
10–100	0.19	2.89
10–200	0.12	4.08
30–100	0.95	0.96
30–200	0.57	1.36

transfer [16].

$$SMD = \frac{0.585}{U_R}\left(\frac{\sigma_L}{\rho_L}\right)^{0.5} + 53\left(\frac{{\mu_L}^2}{\sigma_L \rho_L}\right)^{0.225}\left(\frac{Q_L}{Q_A}\right)^{1.5} \quad (1)$$

where U_R is the relative velocity of air to liquid, σ_L is the liquid surface tension, ρ_L is the liquid density, μ_L is the liquid viscosity and Q_L and Q_A are the volumetric flow rate of the liquid and air, respectively.

On the other hand, the air/liquid mass ratio (ALR) for a nozzle diameter of D = 1.1 mm, were calculated at different mass flow rates of starting solution and dispersion gas, having water and air as fluids by using the Eq. (2) [17]. The ALR must be between 0.1 and 10, since lower values will not produce proper drops, while higher values waste energy [16]. The SMD and ALR values for the pressure of dispersion and feed flow rates combinations used in the experimental matrix are shown in Table 2.

$$ALR = \frac{\dot{m}_{air}}{\dot{m}_{liq}} \quad (2)$$

where, $\dot{m}$ is the mass flow rate and ALR is the air/liquid mass ratio.

Fig. 2 shows the scheme of the synthesis equipment, its parts and where the formation of the nanoparticles takes place. For this, the transformation stages that the droplet goes through during the synthesis process are outlined. The reactor for production of nanoparticles by flame spray pyrolysis is divided in three parts of it: aerosol, burner, and collector system. The aerosol system was defined as an airblast nozzle which shows advantages over other nozzles, since the construction simplicity, the manageability of viscous liquids, the formation of fines spray using low pressures and the low production of soot in the combustion of fuels [16]. The burner system consists in two crossed flames perpendicular to the spray of precursors. To join up the dual-flame burner were used two Victor® torch handles with tips N°1. This kind of tip was chosen because of it allows the minimum flow gases of the Victor® torch handles, allowing a lower gases consumption during the synthesis process. The delivery pressure of the cylinders was choose following the specifications in the torchers manual as 35 psi for O_2 and 7 psi for C_2H_2 [18]. To collect the nanoparticles was made a tubular electrostatic precipitator of aluminum because of its durability, availability, thermal and electrical conductivity. The precipitator was formed by four tubes of 75 cm of length and 7.6 cm of diameter, resulting in a specific collecting area of 0.72 m^2.

Table 3
Factors and levels of the parameters in the experimental design.

Process parameters	Levels	
	Low level	High level
Ceramic loading (%)	2.5	5
Pressure of dispersion gas (kPa)	100	200
Feed flow rate (mL/min)	10	30
Solvent	Ethanol:Water (E)	Methanol:Ethanol:Water (M)
Dispersion gas	Oxygen (O)	Air (A)

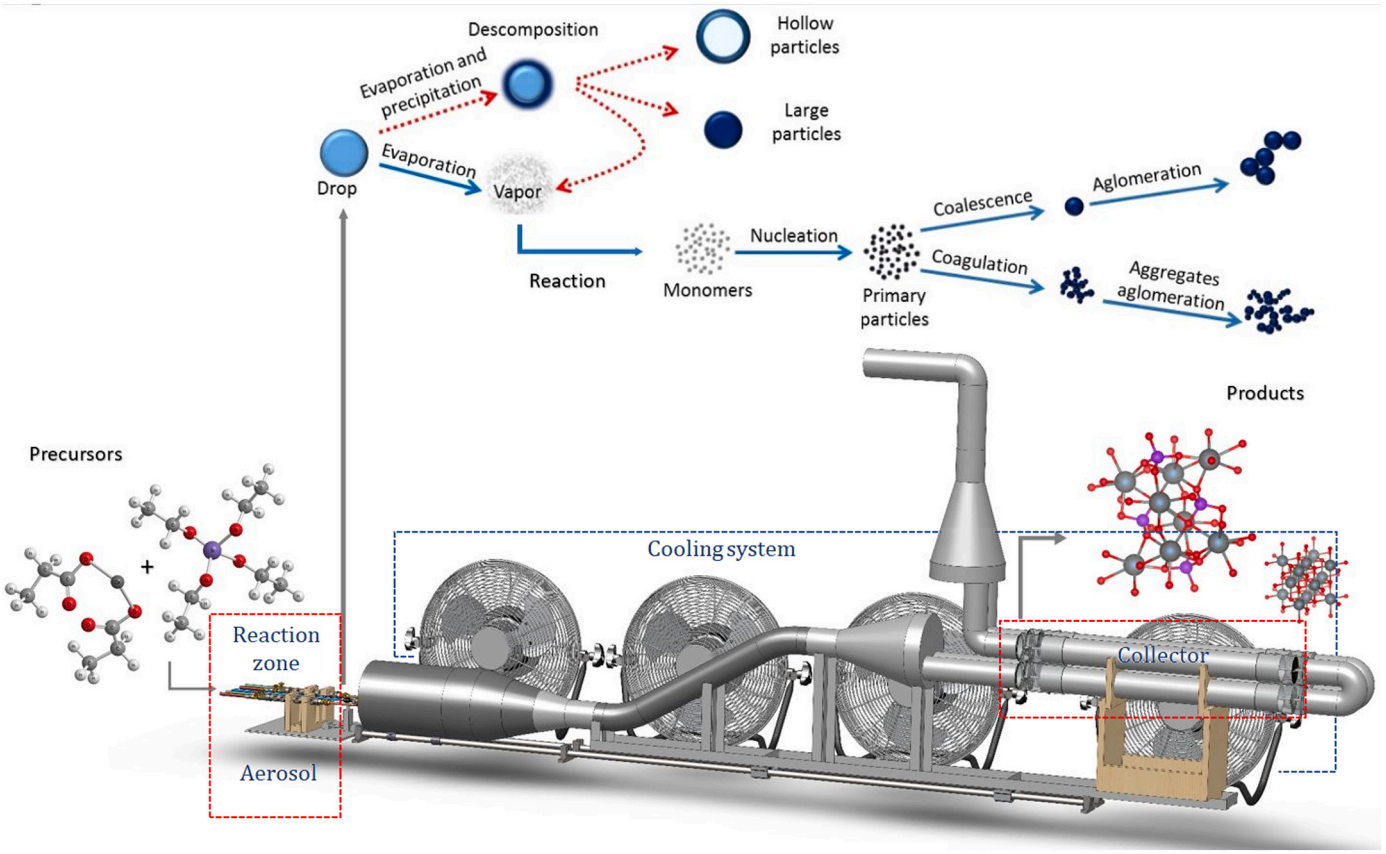

Fig. 2. Experimental setup of the equipment and stages of particle formation.

Table 4
Experimental matrix for the factorial design.

Compound name	Feed rate (mL/min)	Mixture of solvents	Ceramic loading (weight %)	Dispersion gas	Dispersion pressure (kPa)
$30E_{5\%}$-A_{100}	30	E	5	Air	100
$30E_{2\%}$-O_{200}	30	E	2.5	Oxygen	200
$30M_{2\%}$-O_{100}	30	M	2.5	Oxygen	100
$10M_{2\%}$-A_{200}	10	M	2.5	Air	200
$10M_{5\%}$-O_{100}	10	M	5	Oxygen	100
$30M_{5\%}$-A_{200}	30	M	5	Air	200
$10E_{5\%}$-O_{200}	10	E	5	Oxygen	200
$10E_{2\%}$-A_{100}	10	E	2.5	Air	100
$30E_{5\%}$-$A_{100}R$	30	E	5	Air	100
$30M_{5\%}$-$A_{200}R$	30	M	5	Air	200
$10M_{2\%}$-$A_{200}R$	10	M	2.5	Air	200
$10E_{2\%}$-$A_{100}R$	10	E	2.5	Air	100
$10E_{5\%}$-$O_{200}R$	10	E	5	Oxygen	200
$10M_{5\%}$-$O_{100}R$	10	M	5	Oxygen	100
$30E_{2\%}$-$O_{200}R$	30	E	2.5	Oxygen	200
$30M_{2\%}$-$O_{100}R$	30	M	2.5	Oxygen	100

(e.g.: Sample $30E_{5\%}$-A_{100}: solution sprayed at 30 mL/min in ethanol (E) with a concentration of 5 %, and air (A) as dispersion gas at 100 kPa.)

2.3. Design of experiments

To evaluate the interaction effects and the main effects of the process parameters in the formation of the belite phases, an experimental design, a two-level fractional factorial experimental design, resolution III, 2^{5-2} with one repetition, was used. The process parameters evaluated, and their low and high levels are shown in Table 3, while the design responses were the phase compositions obtained by Rietveld refinement, the specific surface area of the powders obtained by BET, and the reactivity of the samples evaluated by microcalorimetry.

In Table 4 is shown the experimentation matrix, randomly defined using the statistical software Minitab®. The matrix is made up of a total of 16 experimental runs to obtain belite samples, composed of 8 samples and 8 replicates for validation of the statistical results.

2.4. Analytical techniques

2.4.1. X-ray diffraction

X-Ray diffraction patterns of anhydrous and hydrated samples were carried out in an PANalytical EMPYREAN X-ray diffractometer, with an X'Celerator detector Bragg Brentano geometry (CuKa $\lambda = 1.5418$ Å) operated at 45 kV / 40 mA (1800 W), with a diffraction interval between 5 and 70° (2θ), with steps of 0.013° (2θ) and time per step of 38 s. The software X'Pert-HighScore plus was used to identify the crystalline phases and quantified by Rietveld refinement as-prepared and with internal standard of rutile (15 %) to determine the fraction of amorphous material, using the free GSAS software. The amorphous fraction was calculated by the spiking method by the over- estimation of an internal crystalline standard using the Eq. (3) [19].

$$ACn\ (\%) = \frac{1 - W_s/R_s}{100 - W_s} x10^4 \quad (3)$$

where W_S (%) is the weighed concentration of the internal standard and R_S (%) is the over-estimate value during the Rietveld analysis [19].

2.4.2. Fourier transform infrared spectroscopy (FT-IR)

Fourier transform infrared spectroscopy (FT-IR) measurements were carried out under ambient conditions in a Shimadzu FT-IR spectrometer (model IRTracer-100 and model FTIR 8400S) between 400 cm^{-1} to 4000 cm^{-1} (spectral resolution 2 cm^{-1}) to obtain chemistry qualitative information of anhydrous samples.

2.4.3. Thermal analysis (TGA)

Thermal analysis of the samples was carried out from room temperature to 1000 °C in a thermobalance STA 449 F3 Jupiter® Netzsch, equipped with two furnaces on a double hoisting gear, coupled with a FT-IR unit of Bruker Optics and a mass spectrometer of Netzsch.

2.4.4. Transmission Electron Microscopy (TEM)

TEM micrographs were carried out in a JEOL JEM-2100 equipped with a field emission cannon (FEG) and a high-resolution CCD camera (Gatan).

2.4.5. Brunauer-Emmett-Teller (BET) surface area

A Flowsorb II 2300 with multigas manifold was used to measure the specific surface area (SSA), by determining the quantity of gas adsorbed as a single layer of molecules on the sample, by the single point procedure, using a Nitrogen:Helium mixture of 30:70 (% volume) and a cold bath of liquid nitrogen.

2.4.6. Isoperibolic calorimetry

The calorimetry measurements were carried out in an isoperibol arrangement equipped with three measuring stations and one reference station. During the measurements, 0.2000 g of each sample was weight and deposit in cupper vials. After 24 h of stabilization, the samples were hydrated with deionized water using a water/solid (w/s) ratio of 5.0, without stirring.

3. Results and discussion

3.1. Mineralogical analysis

The experimental matrix to evaluate the effect of the process parameters on the production of belite phases results in the formation of 16 samples synthesized from the same stoichiometry (Table 2), with clear differences in the mineralogy, indicating a strong effect of process conditions.

The diffraction patterns of the eight main experimental runs of the design and their replication (R) were graphed overlade (Fig. 3). The diffractograms show two clear tendencies of the samples, with well-defined peaks in the diffraction pattern, which will be treated as high crystallinity samples (upper part), and broad peaks with a high noise level treated as low crystallinity samples (bottom). Thus, the synthesis conditions affect not only the phases formed but also their degree of crystallinity since the time in the flame depends on it. Additionally, it is observed the coherence between the original run and the replication, indicating the reproducibility of the method during the synthesis processes.

The samples show the presence up to five crystalline phases and the formation of a hump, which indicates the presence of non-diffracting material, as it was expected considering the particle size of the samples. The phases identified correspond to α-Ca_2SiO_4 (ICSD-81097), β-Ca_2SiO_4 (ICSD-245076- ICSD-245078 and ICSD-79550), $CaCO_3$ (ICSD-80869), CaO (ICSD-90486 and ICSD-51409) and $Ca(OH)_2$ (ICSD-202225, ICSD-202226 and ICSD-34241), where the $CaCO_3$, CaO and $Ca(OH)_2$ will be called secondary phases, considering the quantities of them and their undesired formation. The major components after the amorphous material are the dicalcium silicate polymorphs with peaks between 31 and 34°(2θ) and the calcium carbonate with a main peak ~29°(2θ).

Rietveld refinement was used to quantify the phases in the samples

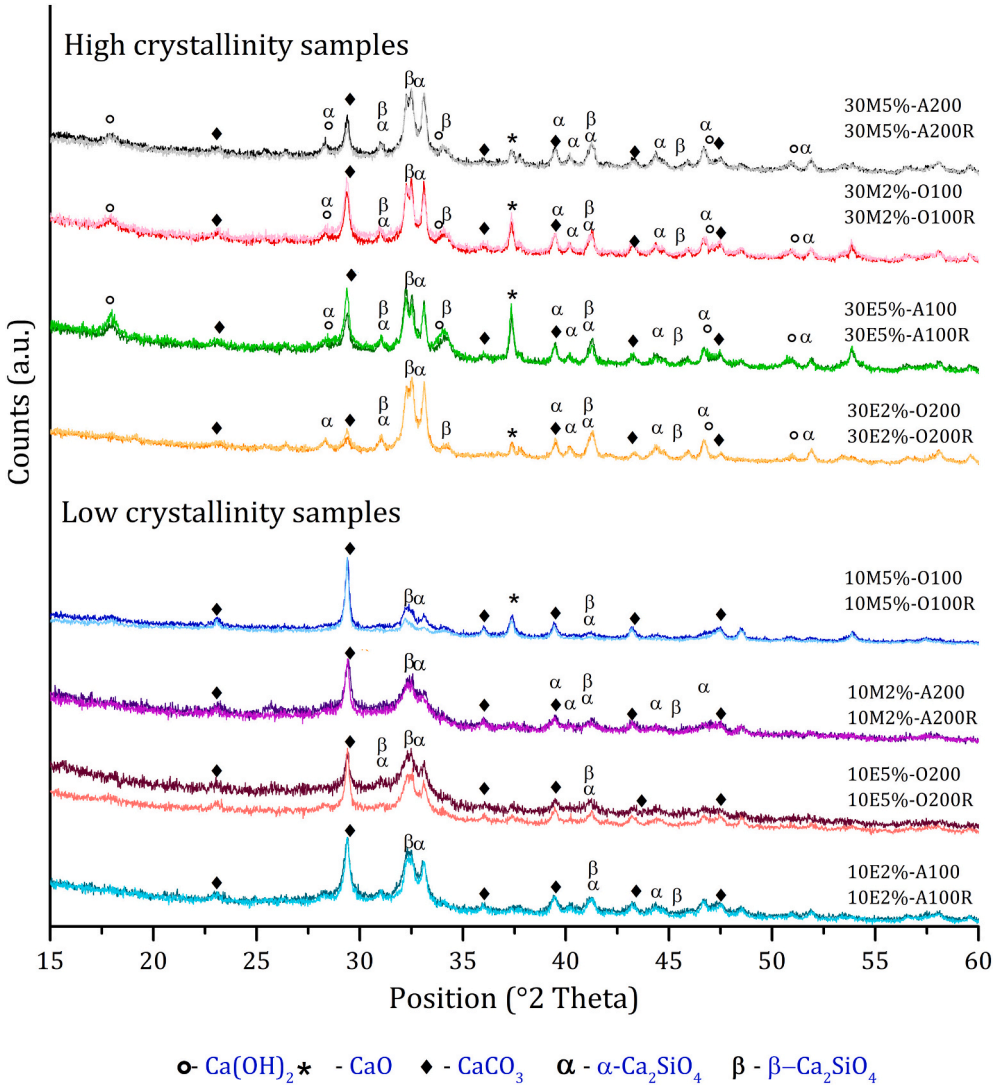

Fig. 3. XRD diffraction patters of anhydrous phases obtained by FSP.

Table 5
Rietveld refinement of the calcium silicate phases with internal standard of rutile.

Sample	Rwp	Amorphous (%)	α-C_2S (%)	β-C_2S (%)	$CaCO_3$ (%)	$Ca(OH)_2$ (%)	CaO (%)
$30M_{5\%}$-A_{200}	7.5	48.1	20.3	19.3	7.2	3.5	1.6
$30M_{5\%}$-$A_{200}R$	6.8	41.1	23.9	22.0	5.9	5.4	1.7
$30M_{2\%}$-O_{100}	7.5	46.2	20.2	17.0	9.8	4.8	2.0
$30M_{2\%}$-$O_{100}R$	7.4	50.7	21.3	8.4	10.9	6.1	2.6
$30E_{5\%}$-A_{100}	6.8	49.0	13.8	21.5	6.2	6.4	3.1
$30E_{5\%}$-$A_{100}R$	7.4	56.1	7.7	17.2	8.5	9.4	1.1
$30E_{2\%}$-O_{200}	7.9	31.2	34.6	28.1	4.0	–	2.1
$30E_{2\%}$-$O_{200}R$	7.8	33.5	16.7	44.3	4.3	–	1.2
$10M_{5\%}$-O_{100}	7.8	51.7	12.2	12.1	18.3	3.3	2.4
$10M_{5\%}$-$O_{100}R$	7.7	48.5	22.5	1.2	21.3	4.9	1.6
$10M_{2\%}$-A_{200}	6.80	78.4	12.9	3.8	4.5	–	0.4
$10M_{2\%}$-$A_{200}R$	7.5	77.1	12.3	4.6	6.0	–	–
$10E_{5\%}$-O_{200}	6.77	74.3	16.3	5.6	3.8	–	–
$10E_{5\%}$-$O_{200}R$	7.7	64.5	16.9	7.7	9.4	–	1.5
$10E_{2\%}$-A_{100}	7.4	59.8	16.8	11.0	12.4	–	–
$10E_{2\%}$-$A_{100}R$	7.5	61.0	18.3	12.4	7.9	0.4	–

considering the non-diffracting material or amorphous (Table 5). The samples present a high percent of non-diffracting material, while the crystalline fraction is formed for α-Ca_2SiO_4, β-Ca_2SiO_4, $CaCO_3$, CaO and $Ca(OH)_2$. The R_{wp} obtained from the Rietveld refinement for all the samples were below 10 %, with a good shape of the difference curve (close to flat). The refined overall parameters were phase scale factors, background coefficients, unit cell parameters, zero-shift error, peak shape parameters, and preferred orientation coefficient when it was necessary [20]. The amount of the non-diffracting material was indirectly obtained by the 15 % addition of a crystalline standard of rutile

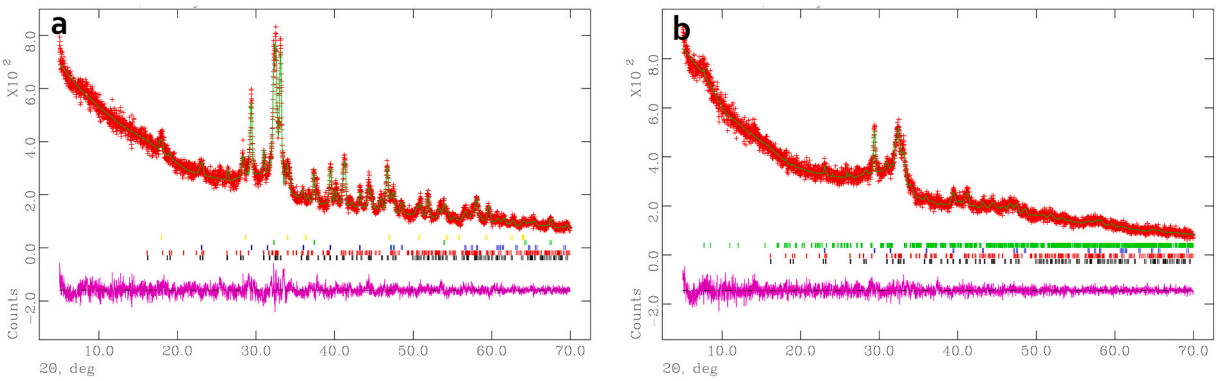

Fig. 4. Rietveld refinement plot of samples a) High crystallinity $30M_{5\%}$-A_{200}, b) Low crystallinity $10E_{5\%}$-O_{200}.

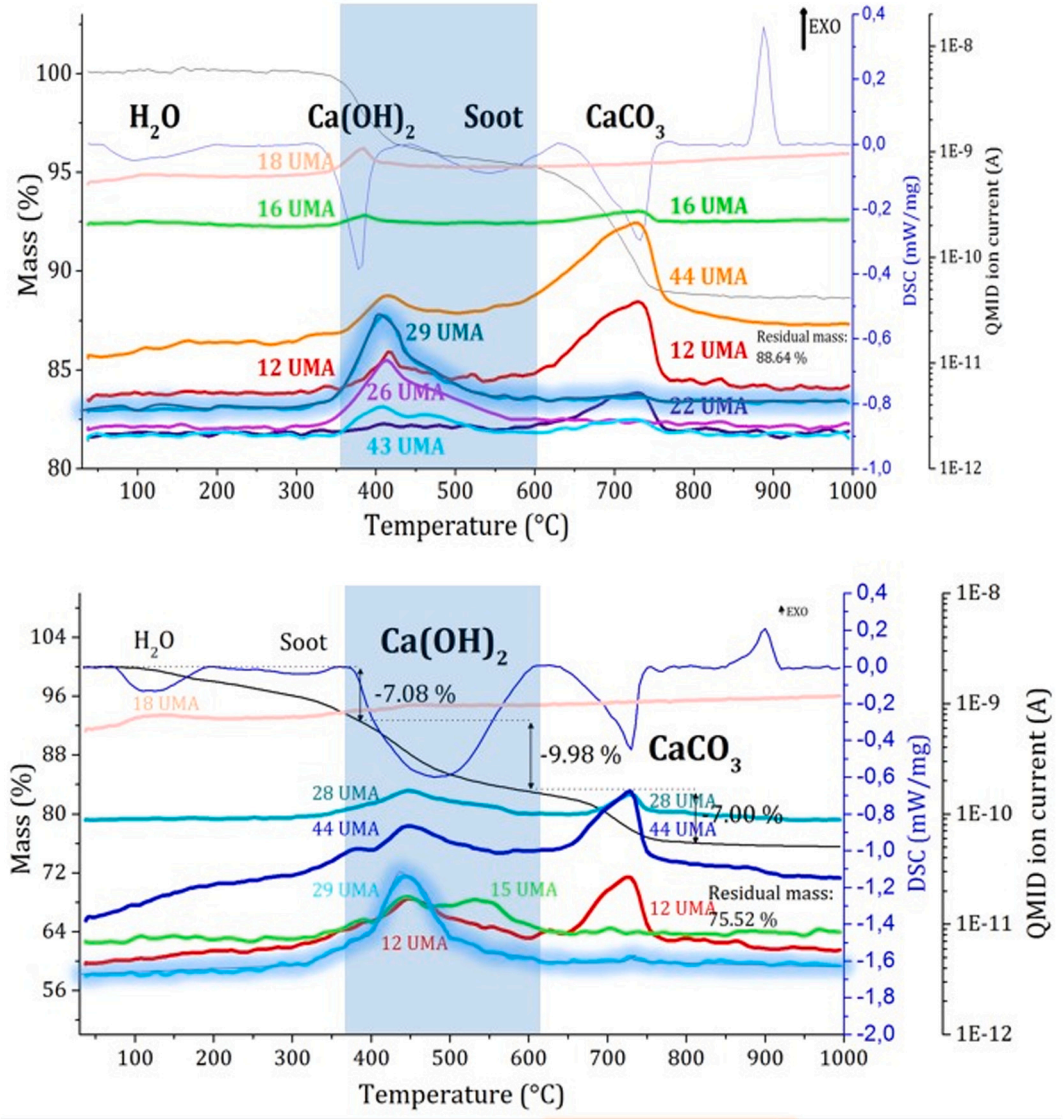

Fig. 5. Thermal analysis coupled to mass spectrometer of a) $30E_{5\%}$-A_{100}; b) $10E_{5\%}$-O_{200}.

(Purity 99.99 %). In Fig. 4 is shown the Rietveld refinement of samples $30M_{5\%}$-A_{200} as representative plot of high crystallinity samples and $10E_{5\%}$-O_{200} for low crystallinity samples.

All the samples present numbers of non-diffracting material with values between 78.3 % and 31.1 %, which can be attributed to amorphous material and nanoparticles of the formed phases, which cannot be detected by XRD. The samples with high crystallinity coincide in being produce using the high level of feed flow rate (30 mL/min), also, presenting higher numbers of unwanted phases as calcium carbonate, calcium hydroxide and calcium oxide. On the other side, the

Table 6
Comparison between thermal decomposition and Rietveld refinement results for secondary phases of the samples.

Sample	$Ca(OH)_2$		$CaCO_3$	
	Rietveld refinement	Thermal analysis	Rietveld refinement	Thermal analysis
$30M_{5\%}$-A_{200}	3.5	3.7	7.2	5.9
$30M_{5\%}$-$A_{200}R$	5.4	3.8	5.9	8.8
$30M_{2\%}$-O_{100}	4.8	4.6	9.8	10.8
$30M_{2\%}$-$O_{100}R$	6.1	4.0	10.9	10.8
$30E_{5\%}$-A_{100}	6.4	4.5	6.2	6.6
$30E_{5\%}$-$A_{100}R$	9.4	7.0	8.5	9.8
$30E_{2\%}$-O_{200}	0.0	0.0	4.0	9.1
$30E_{2\%}$-$O_{200}R$	0.0	2.4	4.3	6.5
$10M_{5\%}$-O_{100}	3.3	7.2	18.3	14.6
$10M_{5\%}$-$O_{100}R$	4.9	14.0	21.3	19.2
$10M_{2\%}$-A_{200}	0.0	5.4	4.5	8.0
$10M_{2\%}$-$A_{200}R$	0.0	10.8	6.0	11.5
$10E_{5\%}$-O_{200}	0.0	10.0	3.8	7.0
$10E_{5\%}$-$O_{200}R$	0.0	9.2	9.4	11.5
$10E_{2\%}$-A_{100}	0.0	8.1	12.4	8.8
$10E_{2\%}$-$A_{100}R$	0.4	5.2	7.9	10.7

Table 7
Percent of calcium oxide formed during the reaction processes.

Sample	Percentages from Rietveld refinement			% CaO produced in the flame
	% CaO	% CaO from $CaCO_3$	% CaO from $Ca(OH)_2$	
$30M_{5\%}$-A_{200}	1.6	4.0	2.6	8.2
$30M_{5\%}$-$A_{200}R$	1.7	3.3	4.1	9.1
$30M_{2\%}$-O_{100}	2.0	5.5	3.6	11.1
$30M_{2\%}$-$O_{100}R$	2.6	6.1	4.6	13.3
$30E_{5\%}$-A_{100}	3.1	3.5	4.8	11.4
$30E_{5\%}$-$A_{100}R$	1.1	4.8	7.1	13.0
$30E_{2\%}$-O_{200}	2.1	2.3	–	4.4
$30E_{2\%}$-$O_{200}R$	1.2	2.4	–	3.6
$10M_{5\%}$-O_{100}	2.4	10.2	2.5	15.1
$10M_{5\%}$-$O_{100}R$	1.6	11.9	3.7	17.2
$10M_{2\%}$-A_{200}	0.4	2.5	–	2.9
$10M_{2\%}$-$A_{200}R$	–	3.4	–	3.4
$10E_{5\%}$-O_{200}	–	2.1	–	2.1
$10E_{5\%}$-$O_{200}R$	1.5	5.2	–	6.7
$10E_{2\%}$-A_{100}	–	6.9	–	6.9
$10E_{2\%}$-$A_{100}R$	–	4.4	0.3	4.7

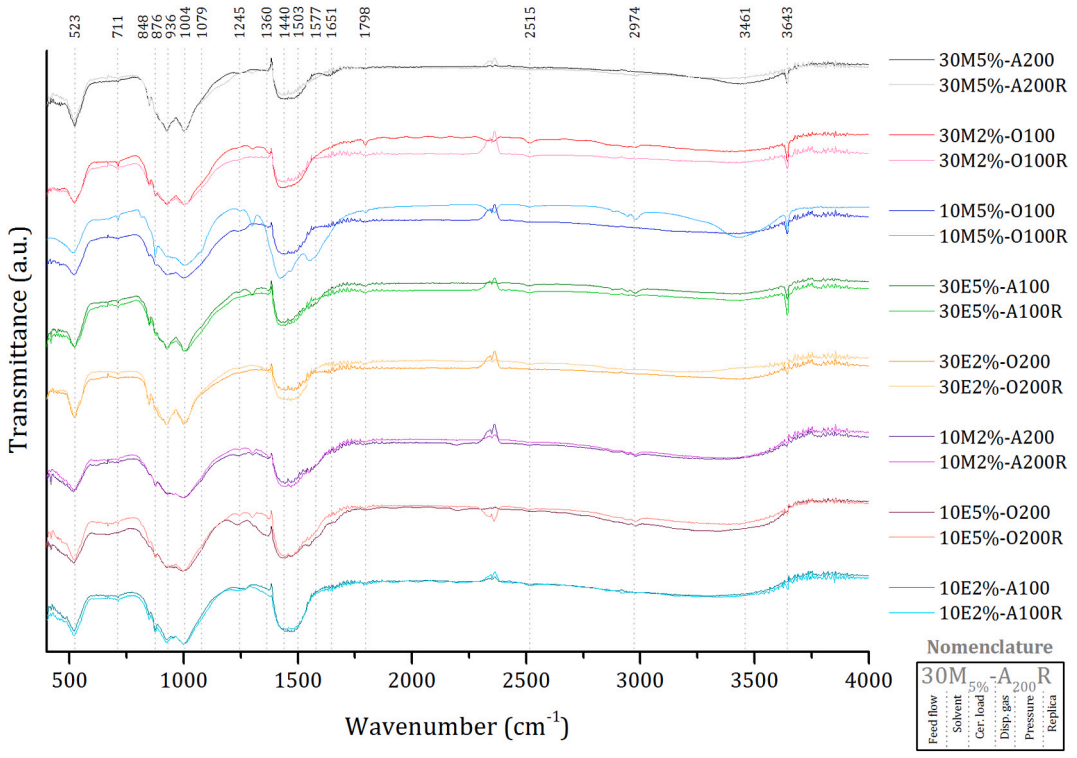

Fig. 6. Fourier transform infrared spectroscopy spectra of anhydrous samples.

Table 8
Specific surface area and average particle size distribution.

Sample	SSA (m^2/g)	APS (nm)
$30M_{5\%}$-A_{200}	31.0	60.5
$30M_{5\%}$-$A_{200}R$	32.6	57.9
$30M_{2\%}$-O_{100}	27.1	69.8
$30M_{2\%}$-$O_{100}R$	28.6	66.6
$30E_{5\%}$-A_{100}	18.0	104.6
$30E_{5\%}$-$A_{100}R$	17.3	110.1
$30E_{2\%}$-O_{200}	34.3	54.3
$30E_{2\%}$-$O_{200}R$	26.2	70.2
$10M_{5\%}$-O_{100}	28.5	68.8
$10M_{5\%}$-$O_{100}R$	19.6	99.2
$10M_{2\%}$-A_{200}	68.6	26.8
$10M_{2\%}$-$A_{200}R$	66.7	27.6
$10E_{5\%}$-O_{200}	49.6	37.1
$10E_{5\%}$-$O_{200}R$	39.8	46.7
$10E_{2\%}$-A_{100}	47.8	39.1
$10E_{2\%}$-$A_{100}R$	38.9	47.7

group of samples with low crystallinity characterized for broader peaks, high percent of amorphous and lower particle size as BET results shown in Table 8 indicates, have in common that they were obtaining with a feed flow rate of 10 mL/min. Of all samples, $10E_{5\%}$-O_{200} presented the lower quantity of calcium carbonate of 3.8 %, indicating that the use of high pressure of dispersion gas and low feed flow rates (10 mL/min - 200 kPa) favors the formation of belite phases. Besides, the combination 30 mL/min - 100 kPa favors the formation of calcium oxide, which is an undesired compound in the samples [3].

With the high feed flow rate is promoted a fast flow of precursors that do not permit a proper evaporation of the droplets, allowing a slow decomposition of the starting solution, which could lead to the formation of heterogeneous products. Furthermore, this leads to the formation of droplets with a higher mean droplet size than low feed streams, especially when combined with a low dispersion gas pressure, increasing the mean droplet size of the aerosol and decreasing droplet kinetics on the fire. This indicates that the relationship of these process parameters play an important role in the mineralogy of the particles.

Phases as $Ca(OH)_2$ and $CaCO_3$ in nanometric size could be

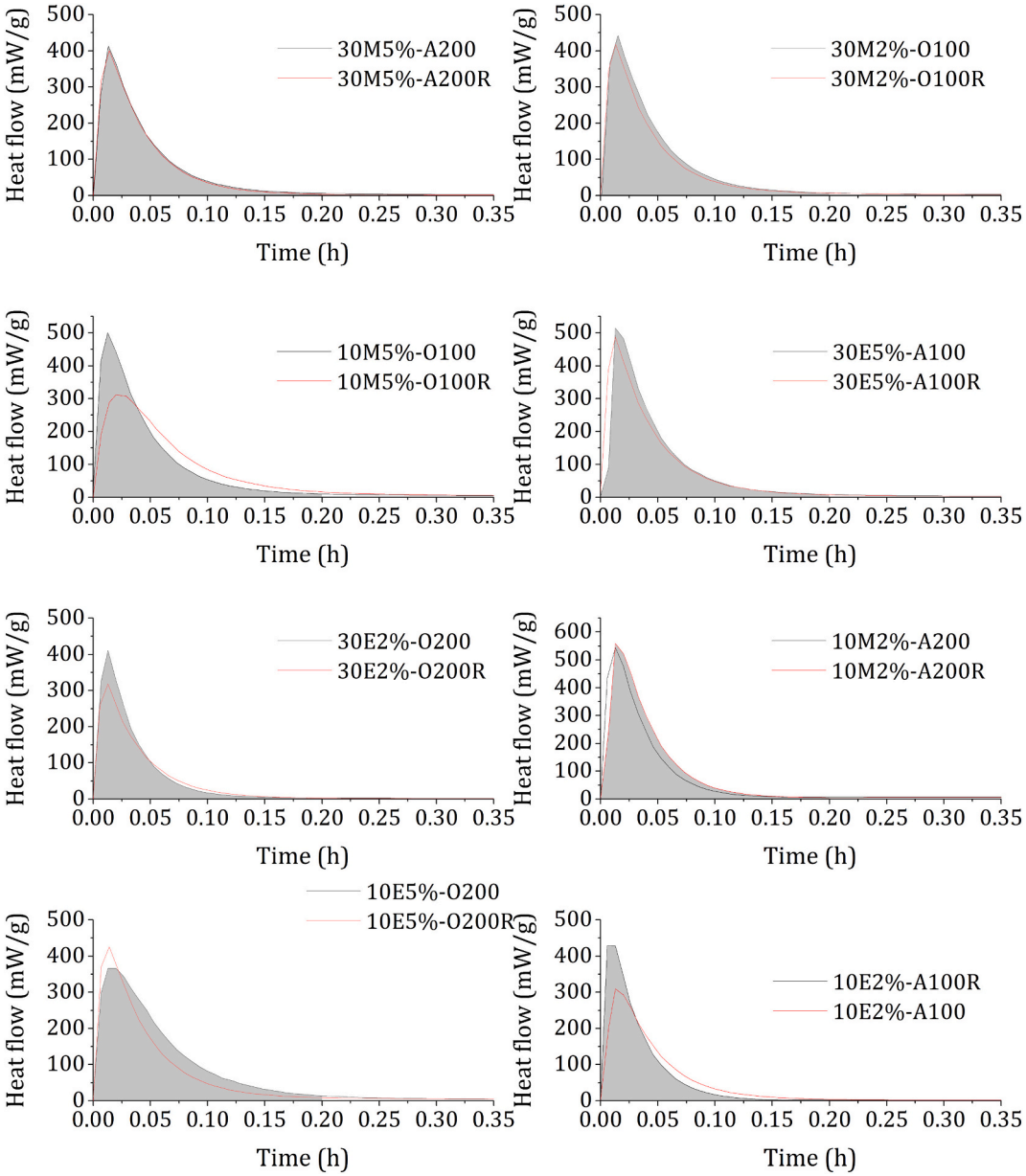

Fig. 7. First peak of heat flow curves of calcium silicates.

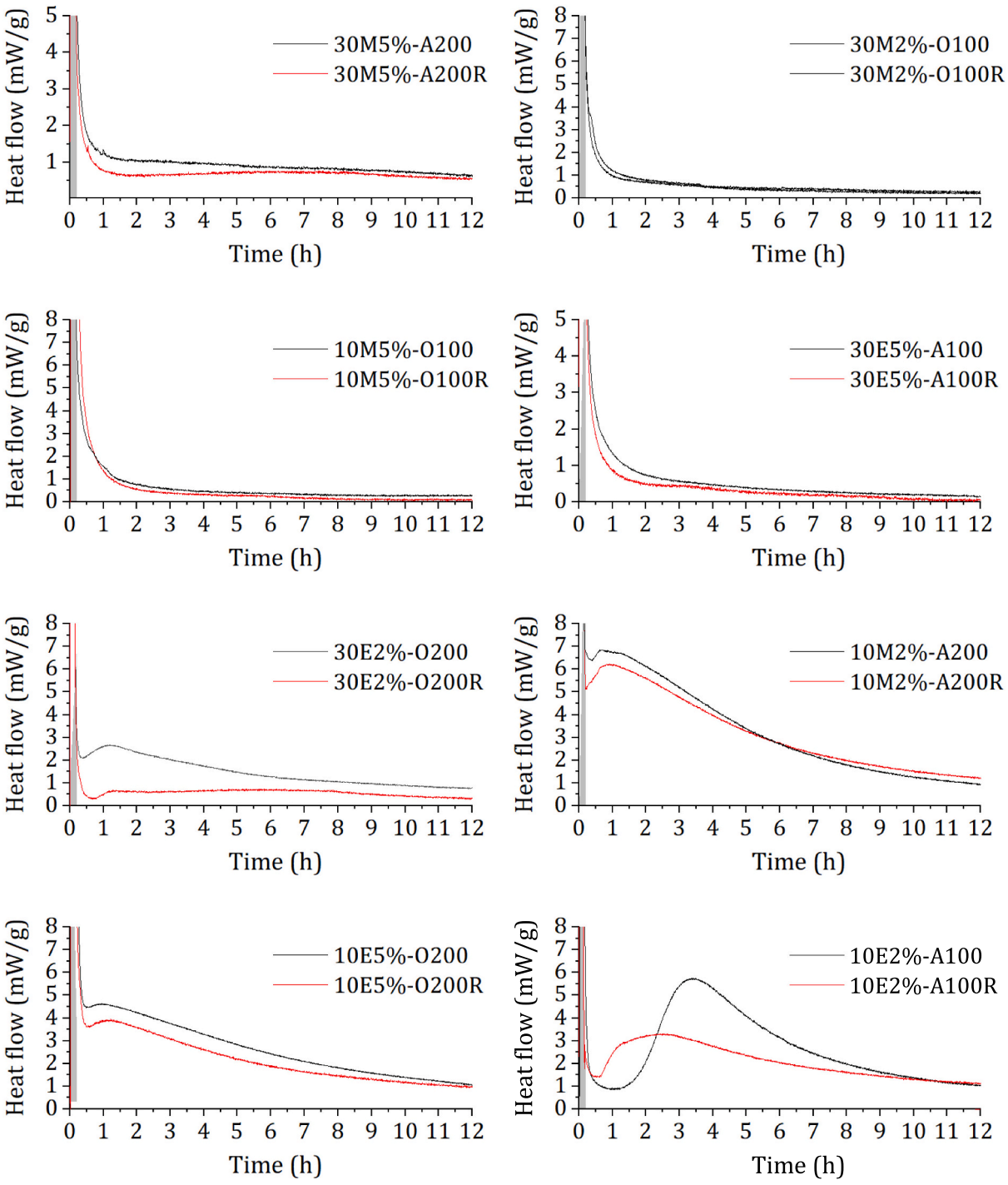

Fig. 8. Second peak of heat flow curves of calcium silicates.

undetectable by XRD analysis, being part of the non-diffracting material, but their identification can be possible by thermal techniques as TGA. Therefore, the samples were submitted to thermal analysis coupled to mass spectrometer and infrared spectroscopy, (TGA/DSC + MS/FTIR) under a nitrogen atmosphere. This technique allows the study of thermal behavior of the samples, giving complementary results to understand and corroborate the Rietveld percentages obtained in the mineralogical analysis. In addition, the use of mass spectrometer and infrared spectroscopy give chemical information about the thermal process of the samples.

In Fig. 5 are presented the TGA-DSC-MS curves of the sample $30E_{5\%}$-A_{100} and sample $10E_{5\%}$-O_{200}. Sample $30E_{5\%}$-A_{100} shows two main losses of mass around 400 °C and 730 °C and three small losses from water and soot in the sample. The gases evolved during the decomposition were identified by mass spectrometry and infrared spectroscopy. The first significant loss of mass between 319 and 416 °C with a value of 3.66 % is associated to the dehydration of portlandite present in the sample. In this range, the mass spectrometer results indicate the release of gases with 16 and 18 UMA attributed to the hydroxyl groups of $Ca(OH)_2$. Two small losses of mass of 1.03 % and 0.99 % are produced around

Table 9
Heat flow released during the hydrolysis of calcium silicates.

Sample	First peak		Second peak	
	Max height (mW/g)	Heat flow (mJ/g)	Max height (mW/g)	Heat flow (mJ/g)
$30M_{5\%}$-A_{200}	413.02	18.88	1.07	15.57
$30M_{5\%}$-$A_{200}R$	400.49	18.36	0.81	13.71
$30M_{2\%}$-O_{100}	441.89	20.89	0.82	6.62
$30M_{2\%}$-$O_{100}R$	417.83	19.01	0.73	7.35
$10M_{5\%}$-O_{100}	500.37	24.62	1.33	8.95
$10M_{5\%}$-$O_{100}R$	312.08	23.65	0.58	3.21
$30E_{5\%}$-A_{100}	514.11	22.67	0.76	4.94
$30E_{5\%}$-$A_{100}R$	487.32	22.60	0.51	3.08
$30E_{2\%}$-O_{200}	410.34	14.75	2.72	21.95
$30E_{2\%}$-$O_{200}R$	317.73	13.51	0.73	9.88
$10M_{2\%}$-A_{200}	543.71	22.07	6.86	45.58
$10M_{2\%}$-$A_{200}R$	559.32	24.27	6.22	48.10
$10E_{5\%}$-O_{200}	365.87	25.32	4.63	38.46
$10E_{5\%}$-$O_{200}R$	425.58	21.10	3.95	33.21
$10E_{2\%}$-A_{100}	308.78	15.37	5.75	38.90
$10E_{2\%}$-$A_{100}R$	429.11	16.09	3.07	37.48

400–600 °C, in which mass spectrometer signals with 12, 14, 28, 29 and 30 UMA from dissociation of carbon monoxide; these gases could be attributed to the decomposition of residual soot produced during the combustion. The second major loss of mass of 6.68 % is associated with the decarbonation of $CaCO_3$ with a release of gases corresponding to CO_3^{2-} with 12, 16, 22 and 44 UMA, with a remarkable proportion of 44 UMA.

In addition, an exothermic and four endothermic transitions were observed on the heating of the sample. The first endothermic peak is attributed to the evaporation of water in the sample with an energy change of −23.92 J/g. The second endothermic peak corresponding to the decomposition of portlandite with an energy change of −70.63 J/g. The enthalpy changes during the decomposition of calcium carbonate achieve the higher value of −89.85 J/g, and finally, was observed an exothermic peak releasing 39.1 J/g between 864 °C – 915 °C, which could be attributed to a recrystallization of calcium silicates in the sample, considering the availability of amorphous material and calcium oxide from the other decompositions.

In Fig. 5 – b is shown the TGA-DSC-MS curves of the sample $10E_{5\%}$-O_{200}. In this case, the slope of the TGA curve goes down softly, nevertheless, there are also identified two major losses of weight at 400 °C and 730 °C, and three small losses of mass attributed to water, soot, and possible alkyl chains. The first loss of mass of 3.15 % corresponds to the free water evaporation until 250 °C evolving gases with 18 UMA. In this range, the DSC curve shows an endothermic transition with an enthalpy of −59.42 J/g.

Between 260 and 600 °C, a large loss of mass occurs, which can be divided in three overlaid decompositions, which can be identified based on the gases released. The first weight loss between 260 and 390 °C has a value of 3.33 % where are released gases with a 30 UMA possible for alkyl chains decomposition. In this range, the DSC curve shows a small endothermic transition of −13.24 J/g. The second mass loss between 370 and 499 °C, with a value of 8.18 %, cannot be attributed to a single decomposition, because the soot and portlandite decomposed in the same range of temperatures. However, the gases with higher concentration correspond to dehydration reactions by the release of gases with 16, 17 and 18 UMA. In lower concentration were identified gases with 27, 28, 29 and 44 UMA associated to carbon monoxide and carbon dioxide. The third mass loss between 500 and 600 °C, has a value of 2.51 %, in which was identify the release of gases with 15 and 28 UMA, attributed also to soot decomposition. In this broad range, the DSC curve shows a broad endothermic peak with a high enthalpy of −448.2 J/g.

Finally, a second significant loss of mass of 6.23 % occurs between 610 and 750 °C, with an endothermic transition, which releases −117 J/g. In this range were identified gases corresponding to CO_3^{2-} with 12, 22, 28, 29 and 44 UMA, from the decarbonation of $CaCO_3$. An exothermic peak releasing an enthalpy of 32.08 J/g was also observed around 900 °C, probably from a recrystallization of calcium silicates in the sample. These two graphs are used as representative examples of the TGA-DSC-MS curves.

In Table 6 is presented a comparison between the amounts of calcium carbonate and calcium hydroxide obtained by Rietveld refinement and thermal analysis. The slight differences in the percentages of portlandite and calcium carbonate from TGA results and Rietveld refinement can be explained by the formation of nanosized phases, which cannot be identify by XRD, being part of the amorphous and crystalline not-quantified (ACn) material in the samples.

Fourier transform infrared spectra of all the samples are shown in Fig. 6. The IR spectra shown three main bands around 520 cm^{-1} and 950 cm^{-1} belonging to silicate vibrations and 1450 cm^{-1} belonging to carbonate vibrations. Silicate structures present two reflections with maximum values near to 523 cm^{-1} and 1004 cm^{-1}, which correspond to two active frequencies of a tetrahedral group [21–23]. The first band between 430 and 600 cm^{-1}, with a maximum around 523 cm^{-1} is attributed to bending vibrations generated by Si—O—Si [5,24,25]. While, two close bands located in 936 cm^{-1} and 1004 cm^{-1} correspond to symmetrical Si—O stretching vibrations of SiO_4 [26–28], where the band located around 936 cm^{-1} can be attributed to Ca—O—Si vibrations [29] and the band located at 1004 cm^{-1} corresponds to ν_3(Si—O) stretching vibrations [30]. The shoulder located in 1096 cm^{-1} is attributed to Si—O stretching vibrations of amorphous silica, which could be part of the non-diffracting material in the samples [31].

Additionally, all the samples show the presence of the calcite, which is the most stable polymorph of calcium carbonate. The bands located at 711, 873 and 1440 cm^{-1} are attributed to C—O vibrations of CO_3^{2-}ions from ν_4 (doubly degenerate in-plane bending), ν_2 (out-of-plane) and ν_3 (doubly degenerate asymmetric stretching) vibrations of calcite. Also, there are identified minor bands of this polymorph, located in 848 cm^{-1} and 1798 cm^{-1} [32,33]. On the other hand, small bands between 2500 cm^{-1} to 2974 cm^{-1} present in some samples are associated to C—O vibrations of soot as impurities from the combustion processes, like the bands located around 846 and 1245 cm^{-1} [34].

Most of the samples show a broad band located at 3461 cm^{-1}, attributed to stretching vibrations of O—H mainly by the presence of hydroxyl ions from portlandite and absorbed molecular water from the environment, while the small band or in some spectra the small shoulder around 1651 cm^{-1} is attributed to O—H bending vibrations [29,31]. Finally, the sharp band at 3643 cm^{-1} is associated to O—H stretching vibrations from hydroxyl ions of portlandite and hydroxyl ions strongly bound to calcite [33].

Considering the results obtained by XRD, TGA-DSC/MS-IR and FT-IR, it is possible to affirm that the chemical reactions in the processes are defined as in Eqs. (4) to (7) as shown in previous research results [6,15].

$$2Ca(O_2CCH_2CH_3)_2 + Si(OC_2H_5)_4 \xrightarrow{\Delta} a\ (\alpha,\beta)\ Ca_2SiO_{4(c)} + b\ Ca_2SiO_{4(a)} + c\ CaO_{(c)} + d\ SiO_{2(a)} + 4\ C_2H_4 + 2\ H_2O + 2\ C_5H_{10}O + 2\ CO_2 \quad (4)$$

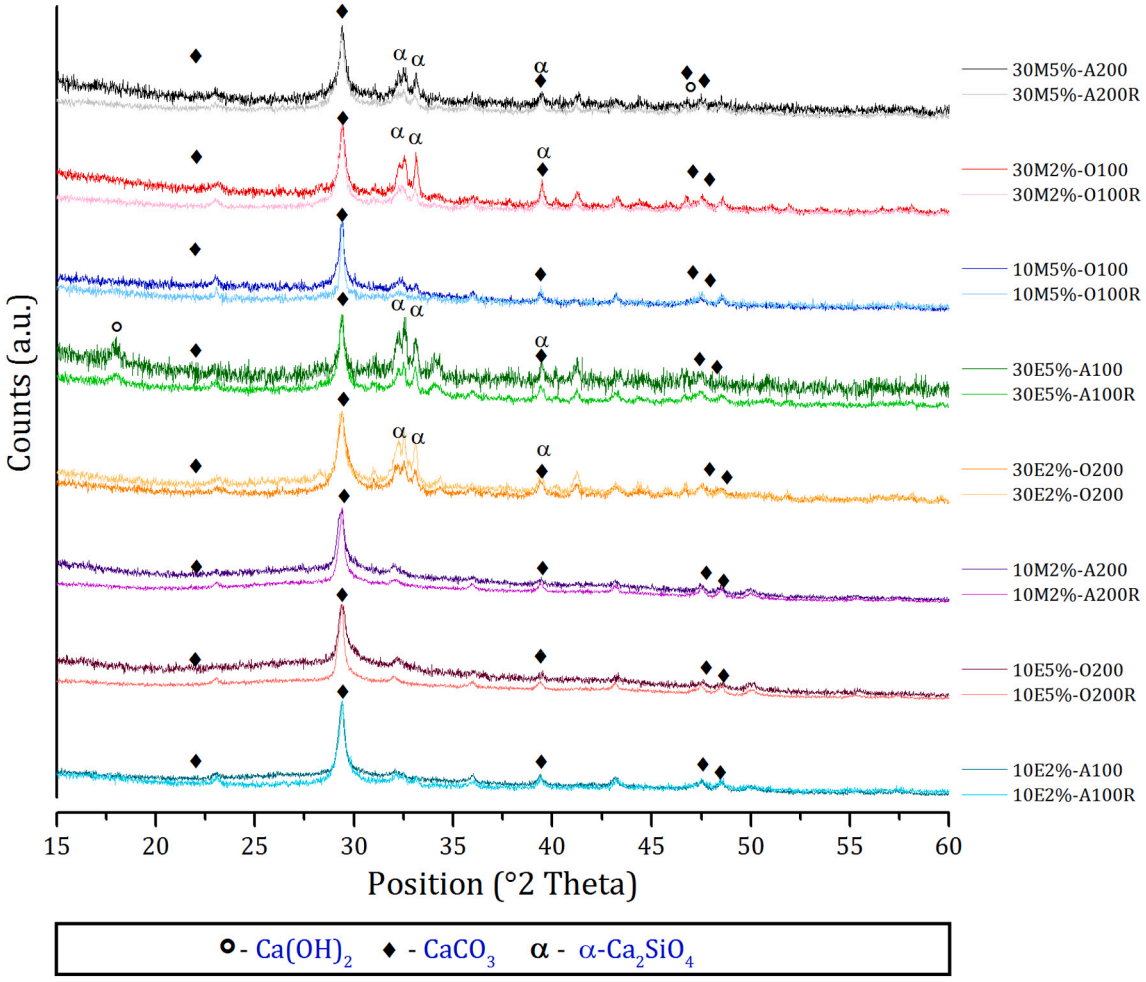

Fig. 9. XRD patterns of the samples hydrated at 2 days.

$$2Ca(O_2CCH_2CH_3)_2 + Si(OC_2H_5)_4 + 26\,O_2 \xrightarrow{\Delta} a\,(\alpha,\beta)\,Ca_2SiO_{4(c)} + b\,Ca_2SiO_{4(a)} + c\,CaO_{(c)} + d\,SiO_{2(a)} + 20\,CO_2 + 20\,H_2O \quad (5)$$

$$CaO + H_2O \rightarrow Ca(OH)_2 \quad (6)$$

$$Ca(OH)_2 + CO_2 \rightarrow CaCO_3 + H_2O \quad (7)$$

Eqs. (4) and (5) show the thermal decomposition and oxidation reactions of the precursors in the flame, respectively, to produce the compounds found in the mineralogical characterization of the samples, where *a, b, c* and *d* represent the stoichiometric coefficients of each product. The characterization shows the formation of calcium oxide, portlandite and calcium carbonate as by-products of the reactions, however, due to the combustion environment and the high reaction temperatures (above 1500 °C) the formation of compounds such as $Ca(OH)_2$ and $CaCO_3$ is not possible in the flame, since high temperatures decompose them. However, the precursors of the reaction can produce polymorphs of dicalcium silicate and CaO, where CaO can react to form $Ca(OH)_2$ and $CaCO_3$ through the precipitator with the conditions of the environment. Under high humidity conditions, from the water vapor released in combustion, CaO particles react with water vapor to form calcium hydroxide as shown in Eq. (6), which in turn reacts with dioxide carbon from the environment to form calcium carbonate as in Eq. (7).

Considering these equations and the chemical data obtained from the Rietveld refinement, the real amount of calcium oxide produced in each reaction was calculated. For this, the calcium oxide necessary to form $CaCO_3$ and $Ca(OH)_2$ was calculated in each reaction and added to the value of calcium oxide from the refinement. The calcium oxide amounts of each reaction are shown in Table 7.

The foregoing makes it possible to state that the secondary phases were constituted by calcium oxide, calcium carbonate and calcium hydroxide. During the flame reaction, the starting solution is decomposed and evaporated, stages in which the components of the new gas phase react to form the nucleus and primary particles. However, some factor as the nature of the starting materials and the solvents used in the reaction can affect the proper formation of this gas phase. The mixture of solvents used to form the starting solution contained water and ethanol, while the precursors were tetraethyl orthosilicate and calcium propionate. These precursors prefer the solvents used, so that tetraethyl orthosilicate dissolves well in ethanol, while calcium propionate, as an organic salt, prefers water as a solvent. Furthermore, TEA was added to the solution to improve its homogeneity and stability. Despite this, the composition of the phases showed that the combination of these precursors needs improvement to avoid the production of unwanted compounds. The evaporation of water demands a greater amount of energy than that of ethanol, therefore, even when the solution looks homogeneous, it could be possible that a higher concentration of silicon ions evaporates more easily due to the affinity with ethanol, leaving higher concentration of calcium ions in the aqueous phase. This concentration of calcium ions in the water will require more time to form an adequate gas phase to react with the silicon ions and form the calcium silicates, so tetraethyl orthosilicate will partially produce amorphous silica and calcium silicates, while calcium propionate will partially produce calcium silicates

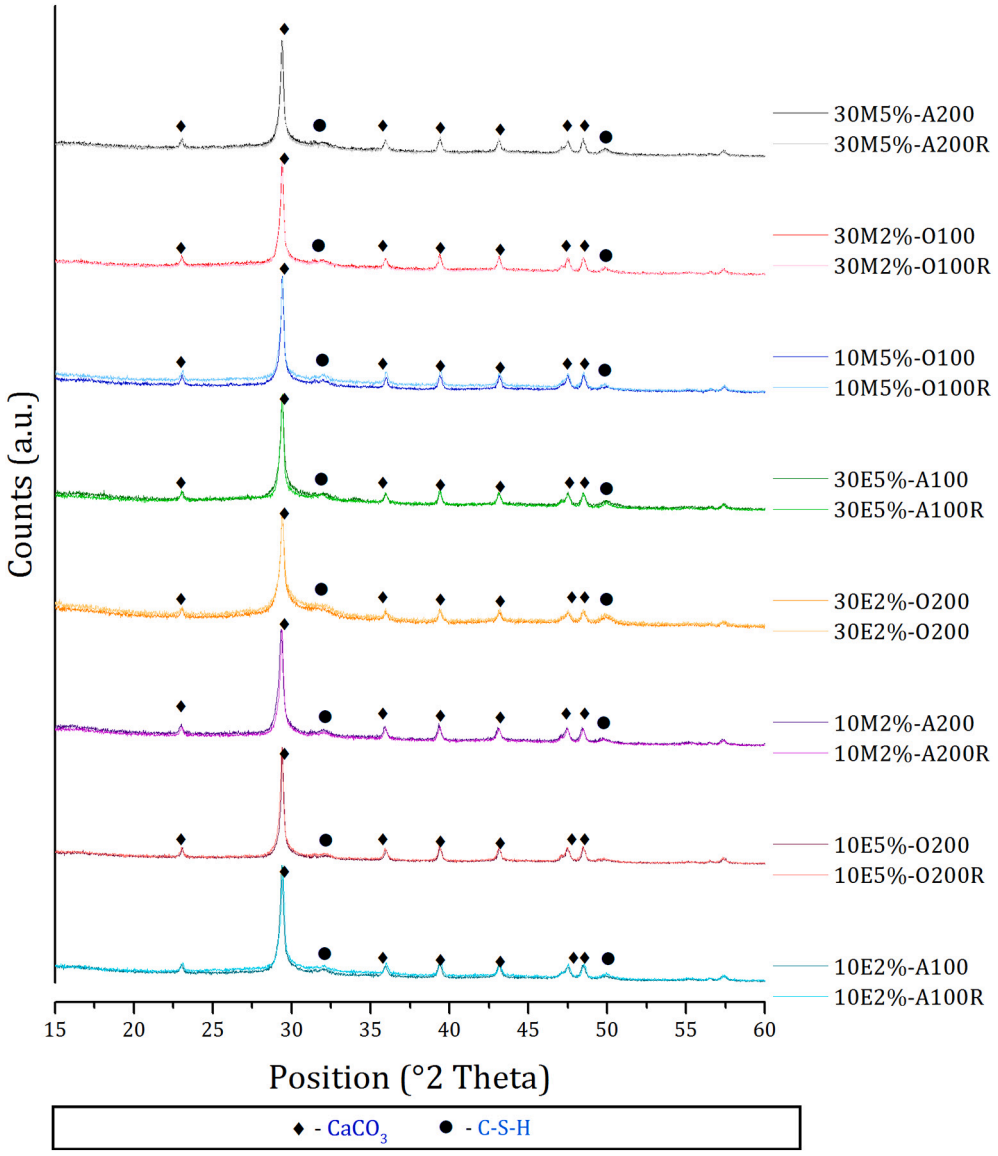

Fig. 10. XRD patterns of the samples after 28 days of hydration.

and calcium oxide. Then, from the calcium oxide formed, the formation of calcite and portlandite occurs when exposed to an environment rich in water vapor and carbon dioxide from combustion, so that the calcium oxide adsorbs moisture to form hydroxide of calcium, which could undergo carbonation reactions to produce calcium carbonate by fixing CO_2.

3.2. Reactivity analysis

C—S—H is the primary bonding phase in portland cement. When producing calcium silicate nanoparticles, the reactivity of the material increases due to the high specific surface area, facilitating the nucleation and growth processes of calcium silicate hydrate (C—S—H) in early stages of hydration [35]. However, this reactivity does not depend only on the specific surface area of the samples, but also on the production of reactive phases with hydraulic properties during the pyrolysis reaction [8,36].

Table 8 shows the results obtained for the specific surface area of the samples. The average particle sizes (APS) of the samples were determinate using the Eq. (8), assuming spherical, monodisperse particles. Where APS is the average particle size, SSA is the specific surface area, x is the mass fraction and ρ is the density of the compound [37].

$$APS = \frac{6}{SSA.\sum(x_i.\rho_i)} \tag{8}$$

The average particle sizes were between 26.8 nm and 110.1 nm, for 10 $M_{2\%}$-A_{200} and 30$E_{5\%}$-A_{100}R, respectively. The samples 10$M_{2\%}$-A_{200}, 10$E_{5\%}$-O_{200}, 10$M_{2\%}$-A_{200}R, 10$E_{2\%}$-A_{100}, 10$E_{5\%}$-O_{200}R and 10$E_{2\%}$-A_{100}R, presented values under 50 nm, while the rest of the samples have a larger size. The standard deviation of the specific surface area of the first run of experiments and their replication are under ± 7 m^2/g, indicating good reproducibility of the results. Results indicate that the samples with higher specific surface area are obtained when the pressure of dispersion gas and feed flow rate take values of 200 kPa and 10 mL/min, respectively. This combination corresponds to an aerosol with smaller mean drop size from the Sauter mean diameter calculations (Table 2). Additionally, the lower specific surface area was obtaining by the combination of 100 kPa and 30 mL/min, corresponding to the bigger droplets in agreement with the Sauter mean diameter, concluding that bigger droplets affect the features of the particles, even when metallorganic compounds with high enthalpy of volatility were used as starting materials.

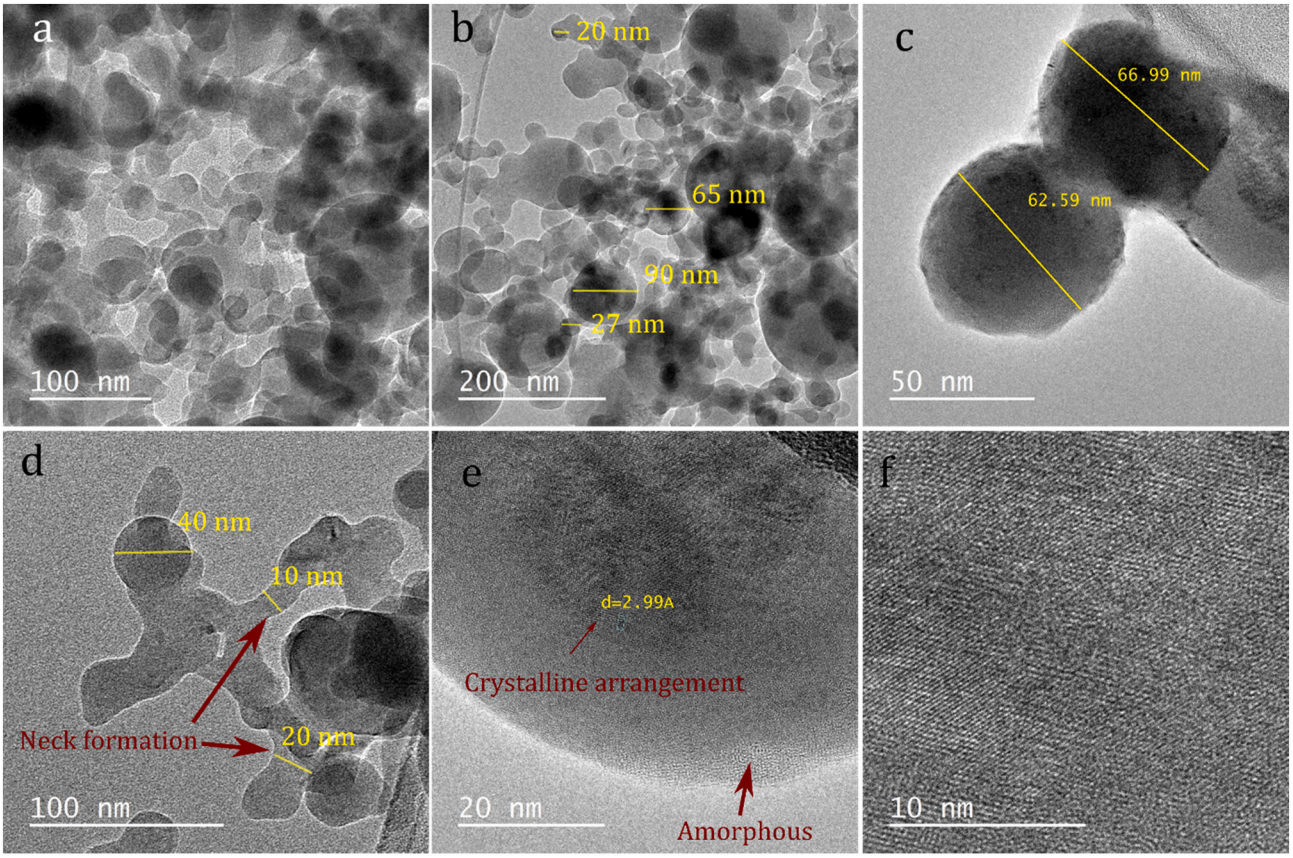

Fig. 11. TEM images of the anhydrous sample $30E_{2\%}\text{-}O_{200}$.

The hydration process is usually divided to four stages, corresponding to the initial period, the induction period, the acceleration period [38,39]. All the samples were submitted under isoperibolic calorimetry to observe their hydration behavior, revealing the complete formation of the initial period after 30 min and the subsequent formation of the second peak with an accelerated behavior. It is known that β-dicalcium silicate present slow reactivity with water, requiring around 28 days to achieve the 30 % of the reaction and 1 year to achieve the 90 %, however the reactivity depends on the surface area of the particles [40].

The area under the curves in Fig. 7 and Fig. 8 represent the cumulative heat flow release during the hydrolysis reaction. The results obtained for each sample in the first and second peaks are presented in Table 9.

In the first peak of hydration take place the dissolution of calcium silicates. The complete formation of this peak took a minimum time of 11 min for the faster reaction and maximum time of 24 min for the slower reaction, achieving the maxima values after 47 s and 2 min of contact with water. The cumulative heat flow released in this stage was between 13.51 and 25.32 mJ/g for samples $30E_{2\%}\text{-}O_{200}R$ and $10E_{5\%}\text{-}O_{200}$, respectively.

The sample $10M_{2\%}\text{-}A_{200}R$ presented the higher maximum height in the first peak with a value of 559.32 mW/g and a cumulative heat flow of 24.27 mJ/g. This sample is one of the samples with the largest amount of amorphous material, low number of secondary phases (6 %) and high surface area (49.6 m^2/g). The replication of this sample present similar response, being the next sample with greater reactivity.

The samples $30M_{5\%}\text{-}A_{200}$, $30M_{2\%}\text{-}O_{100}$, $10M_{5\%}\text{-}O_{100}$ and $30E_{5\%}\text{-}A_{100}$ and their respective replications $30M_{5\%}\text{-}A_{200}R$, $30M_{2\%}\text{-}O_{100}R$, $10M_{5\%}\text{-}O_{100}R$ and $30E_{5\%}\text{-}A_{100}R$ did not show the formation of the second peak after 200 h of reaction, whereby this samples have non-hydraulic behavior after 8 days of reaction. Otherwise, the samples $30E_{2\%}\text{-}O_{200}$ and its replication $30E_{2\%}\text{-}O_{200}R$ present an atypical behavior, due to the second peak of the replication is too small. Similar results were observed in the SSA of these samples, where the sample $30E_{2\%}\text{-}O_{200}R$ has a specific surface area of 26.2 m^2/g, while the original run 34.2 m^2/g. Regarding to the phases identified, both products showed the higher crystallinity and lower amount of amorphous in comparison to the other samples, however, among them were observed differences in the number of polymorphs α-Ca_2SiO_4 and β-Ca_2SiO_4. The total sum of these polymorphs was close, but the amount of α-Ca_2SiO_4 was higher in the most reactive sample ($30E_{2\%}\text{-}O_{200}$), while the amount of β-Ca_2SiO_4 was higher in the replication. These differences in the number of polymorphs and SSA can explain this result, considering that the polymorphs α-Ca_2SiO_4 react faster than β-Ca_2SiO_4 and the SSA was lower for the sample with less heat flow release.

As it was expected, the samples with higher amount of calcium oxide (upon 8 % reported in Table 7), present the lower degree of reactivity due to the percentage of amorphous material and calcium silicates is lower. The sample $30E_{2\%}\text{-}O_{200}R$, was an exception to this behavior, considering that the sample has a low number of secondary phases and a high degree of crystallinity, but the degree of reactivity after 48 h was small.

The samples with higher amount of amorphous material (59.9 %-78.3 %) were $10M_{2\%}\text{-}A_{200}$, $10E_{5\%}\text{-}O_{200}$ and $10E_{2\%}\text{-}A_{100}$ and their respective replications, $10M_{2\%}\text{-}A_{200}R$, $10E_{5\%}\text{-}O_{200}R$ and $10E_{2\%}\text{-}A_{100}R$, which correspond exactly with the samples with hydraulic behavior. The rest of the samples did not show any hydraulic behavior after 8 days of contact with water, which is not presented in the graph in order not to lose resolution in the image, (amorphous percentages between 55 % to 41 %,), except the samples $30E_{2\%}\text{-}O_{200}$ and its replication $30E_{2\%}\text{-}O_{200}R$ (amorphous values around 30 %,), which present a slightly hydraulic behavior.

The curves of the samples with reactive behavior corresponding to

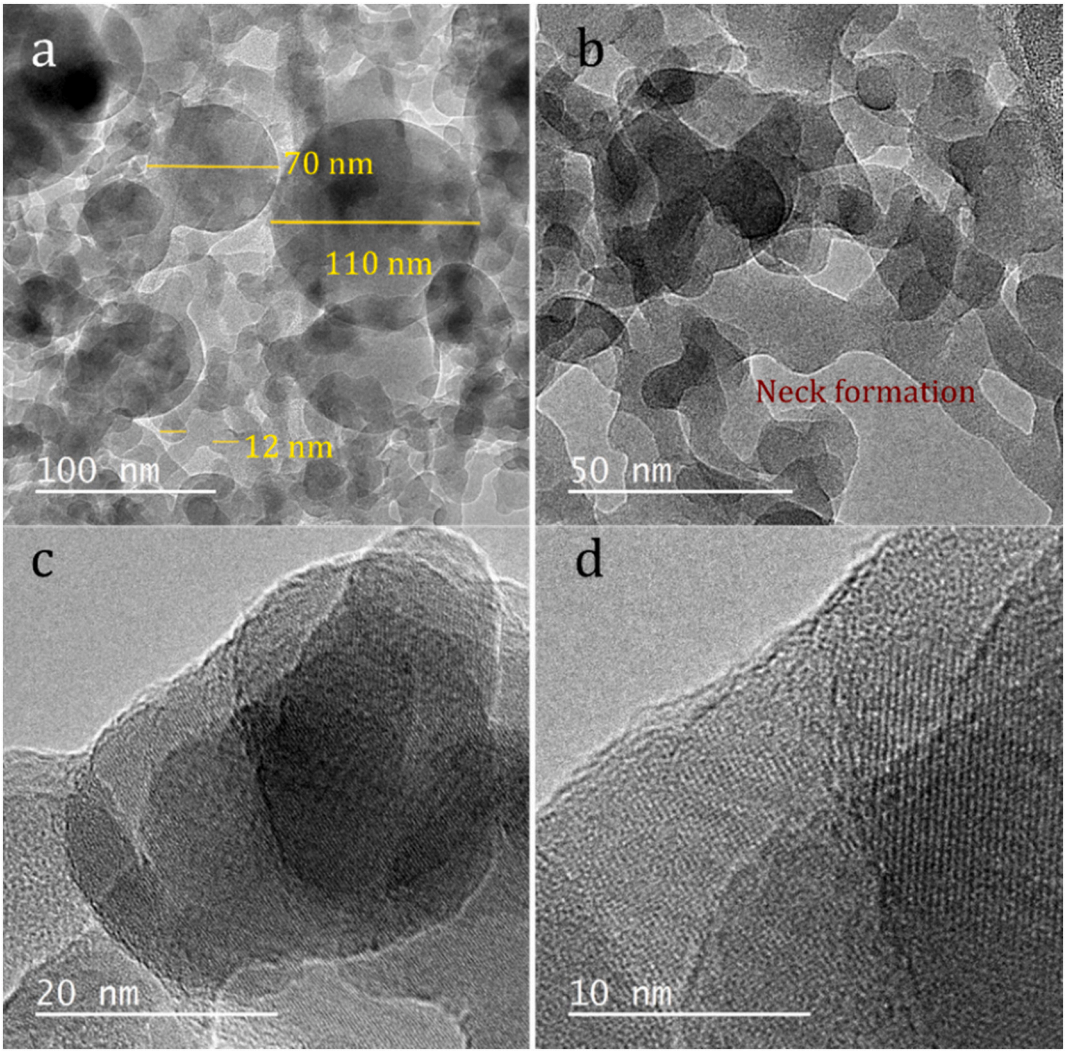

Fig. 12. TEM images of the anhydrous sample $10M_{2\%}$-A_{200}.

$10M_{2\%}$-A_{200}, $10M_{2\%}$-$A_{200}R$, $10E_{5\%}$-O_{200}, $10E_{5\%}$-$O_{200}R$, $10E_{2\%}$-A_{100}, $10E_{2\%}$-$A_{100}R$, $30E_{2\%}$-O_{200} and $30E_{2\%}$-$O_{200}R$ show the formation of a very short or nonexistent dormant period, since the time-consuming nucleation reactions does not have place. These samples start the formation of the second peak after 25 min to 1.5 h of contact with water, achieving the maximum height between 43 min and 4 h. After that, the heat released decrease rapidly until 10 h and continues to decrease gradually until ~40 h.

The amorphous percentage of the samples shows a direct impact on their reactivity, with a stronger effect than the number of belite crystalline polymorphs. The identified amorphous phase is made up of nanometric belite polymorphs which are part of the non-diffractive material due to their size. Nevertheless, samples $30E_{2\%}$-O_{200} and $30E_{2\%}$-$O_{200}R$ are an exception, because were the samples with lower amount of amorphous material, but higher number of polymorphs of belite.

The hydrolysis reactions start at the surface of the samples, controlling the cement hydration kinetics. During the first stage was observed the release of heat from all the samples, which is the result of the dissolution of reactive phases. There is important to notice that most of the samples have a percentage of calcium oxide, which reacts with water in an exothermic process to form portlandite. Then, the reduction in the heat flow after 30 min is observed, where the dormant period was observed only in the sample $10E_{2\%}$-A_{100}. The rest of the hydraulic samples did not show this stage, starting immediately with the formation of hydrolysis products. This behavior indicates that dissolved species in the media, where highly enough to start the nucleation processes required to produce the C—S—H gel. After 48 h of contact with water, all the reactions were stopped, and the hydrated materials were analyzed by XRD (Fig. 9).

All samples contain calcium carbonate after the calorimetry, which was expected due to the unreactive behavior of this phase, which was identified in the un-hydrated samples. The samples $30M_{5\%}$-A_{200}, $30M_{2\%}$-O_{100}, $30E_{5\%}$-A_{100} and $30E_{2\%}$-O200 and their respective replications, $30M_{5\%}$-$A_{200}R$, $30M_{2\%}$-$O_{100}R$, $30E_{5\%}$-$A_{100}R$ and $30E_{2\%}$-$O_{200}R$, show the presence of three peaks between 31.5 and 33.5 (2θ) attributed to dicalcium silicate phases with high crystallinity, which require longer reaction times to react completely with water. These samples showed the lower presence of amorphous material (below 56 %) in comparison with the phases with reactive behavior in which the non-diffraction fraction is upon 61 %. Otherwise, samples $10M_{2\%}$-A_{200}, $10E_{5\%}$-O_{200} and $10E_{2\%}$-A_{100} and their respective replications, $10M_{2\%}$-$A_{200}R$, $10E_{5\%}$-$O_{200}R$ and $10E_{2\%}$-$A_{100}R$, show the presence of calcite and C—S—H (PDF - 33-0306). During the hydration of dicalcium silicates, the reaction products should be calcium silicate hydrate (C—S—H) and calcium hydroxide, however the XRD patterns obtained at 48 h and later ages do not show the presence of calcium hydroxide, which could be carbonated with the exposition to the air. Otherwise, the peaks of dicalcium silicate which did not react correspond to the α-Ca_2SiO_4 phase.

XRD measurements after 28 days of hydration (Fig. 10) reveal a

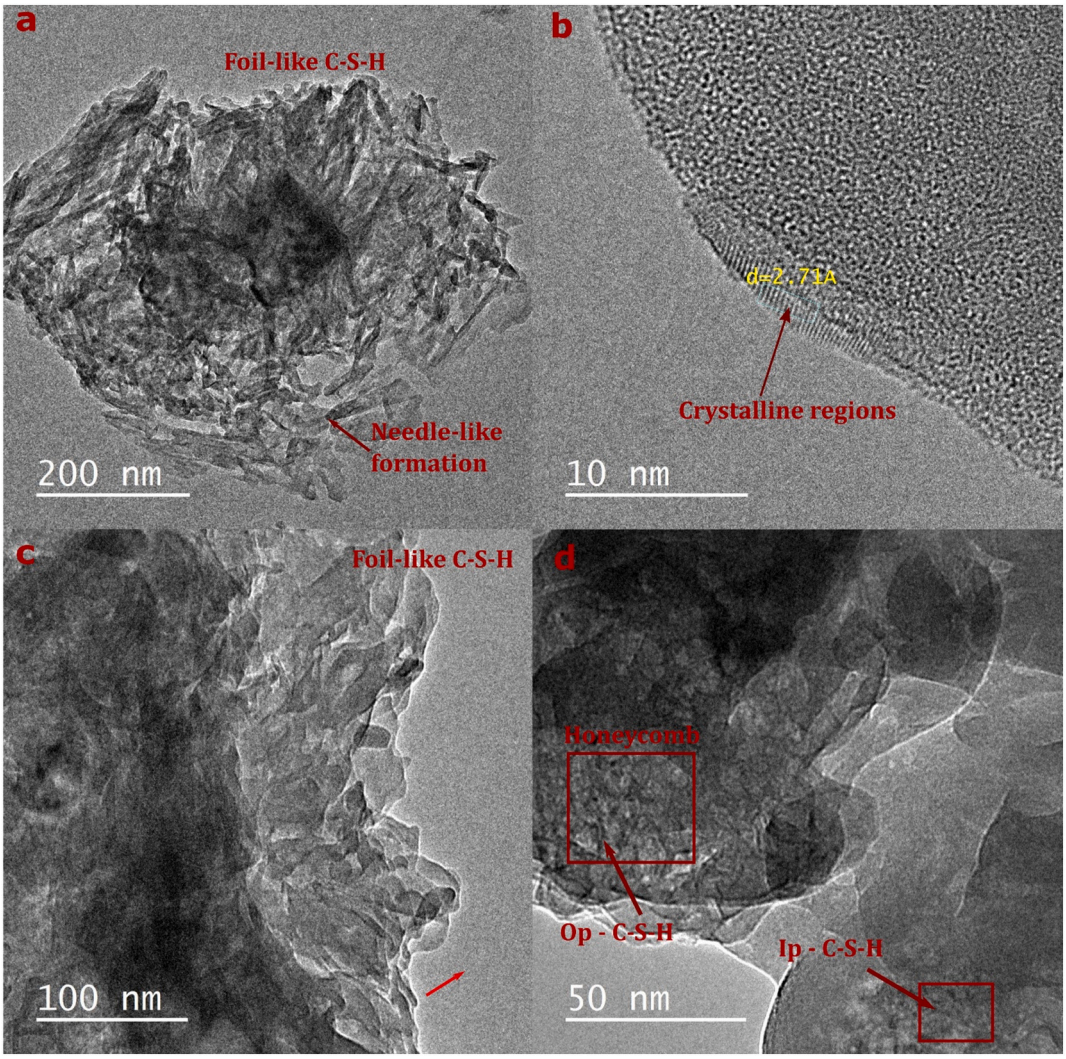

Fig. 13. TEM images of hydrated samples (2 days). (a, b) Sample $30E_{2\%}$-O_{200}; (c, d) Sample $10M_{2\%}$-A_{200}.

complete reaction of all the products, indicating that the two groups of samples (early-reactive and late-reactive) present different kinetics during the hydration. The diffractograms show a clear presence of calcium carbonate and the formation of the three peaks C—S—H around 29°(2θ), 32°(2θ) and 50°(2θ) [41].

TEM images of samples $30E_{2\%}$-O_{200} and $10M_{2\%}$-A_{200} as-prepared and after hydration are shown below. Considering XRD results of anhydrous phases, sample $30E_{2\%}$-O_{200} showed the higher crystallinity regarding to the rest of the samples, while sample showed the higher number of amorphous phase or ACn content. In Fig. 11 are shown TEM images of anhydrous $30E_{2\%}$-O_{200}. In images ***a*** and ***b*** are observed the formation of nanoparticles with spherical shape and irregular aggregates formed by sintering of them. There is observed a broad particle distribution with diameters between 20 nm to 90 nm. The formation of necks (Image ***d***) could be attributed to the high temperature of the oxy-acetylene flame, which promotes sintering processes at the beginning of the synthesis process. These necks were also observed in samples made with a feed flow rate of 10 mL/min, whereby the flame may be the most relevant factor in this growth phenomenon. Images ***e*** and ***f*** show higher magnifications of a particle, in which is possible to observe its atomic arrangement. This particle (Image ***e***) shows highly ordered arrays close to the center which indicate a crystalline arrangements of the atoms, while in the border it is mainly amorphous. The crystalline section is detailed in Image ***f***, in which the good long-range ordering with regular arrays is clearly observed.

In Fig. 12 are observed the TEM images of $10M_{2\%}$-A_{200}.Like $30E_{2\%}$-O_{200}, $10M_{2\%}$-A_{200} shows a broad particle size distribution in nanometric scale, but for this sample, the number of smaller particles is higher, coherently with the specific surface area and calorimetric results (Fig. 12 - *(a)*). In addition, in the image ***b*** is shown the formation of necks between particles with sizes between 10 and 20 nm, increasing the porosity of the sample, which increase the reactivity of the sample, but can decrease the mechanical behavior of the sample after hydration. In the images ***c*** and ***d*** is shown higher magnifications of the particles, in which is observed an ordered pattern of atoms. However, not all the particles and not all the area of each particle show the same pattern.

In Fig. 13 are shown the TEM images of samples $30E_{2\%}$-O_{200} ***(a, b)*** and sample $10M_{2\%}$-A_{200} (***c, d***) after hydration. The images reveal the formation of C—S—H foil-like, but some differences between the samples are observed. Sample $30E_{2\%}$-O_{200} shows the formation of fibrous shape in all the area (image ***a***), with prevalent formation of outer product (OP) C—S—H observed in the formation of needle-like and layered foils, characteristics of early hydration reactions. Higher magnifications (image ***b***) of this sample exhibits a low degree of crystallinity by a random distribution of the dots, suggesting long-range disorder (Image ***c***), while the borders show the presence of crystalline regions with interplanar distances of 2.71 A, which can be attributed to the formation of small nanocrystallites dispersed in the amorphous matrix. Similarly, the sample $10M_{2\%}$-A_{200} shows foil-like morphologies (image ***c***), but higher magnifications reveal the presence of reticular networks

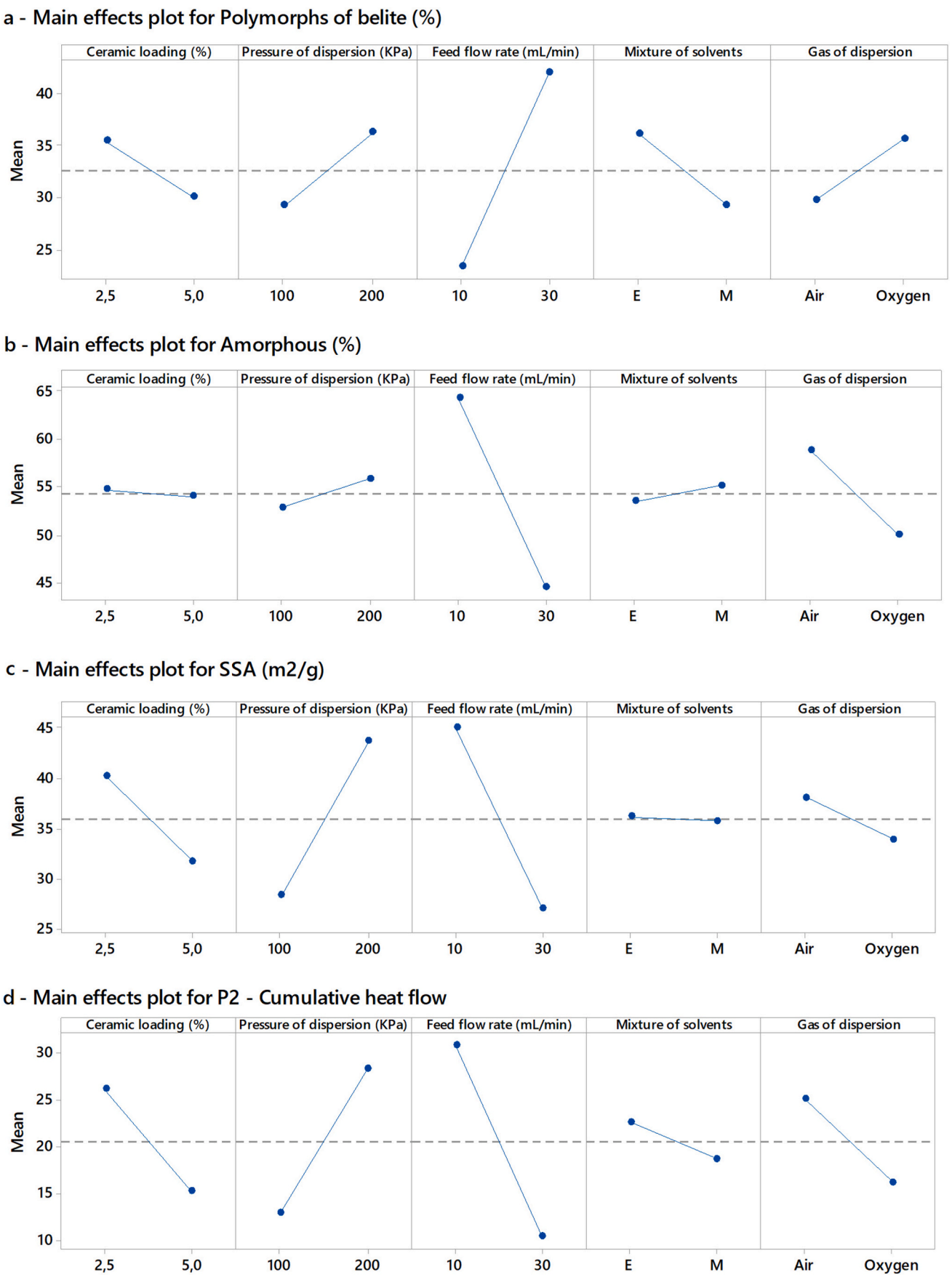

Fig. 14. Main effects of the factors studied on the response variables a) Polymorphs of belite; b) Amorphous phases; c) Specific surface area; d) Cumulative heat flow.

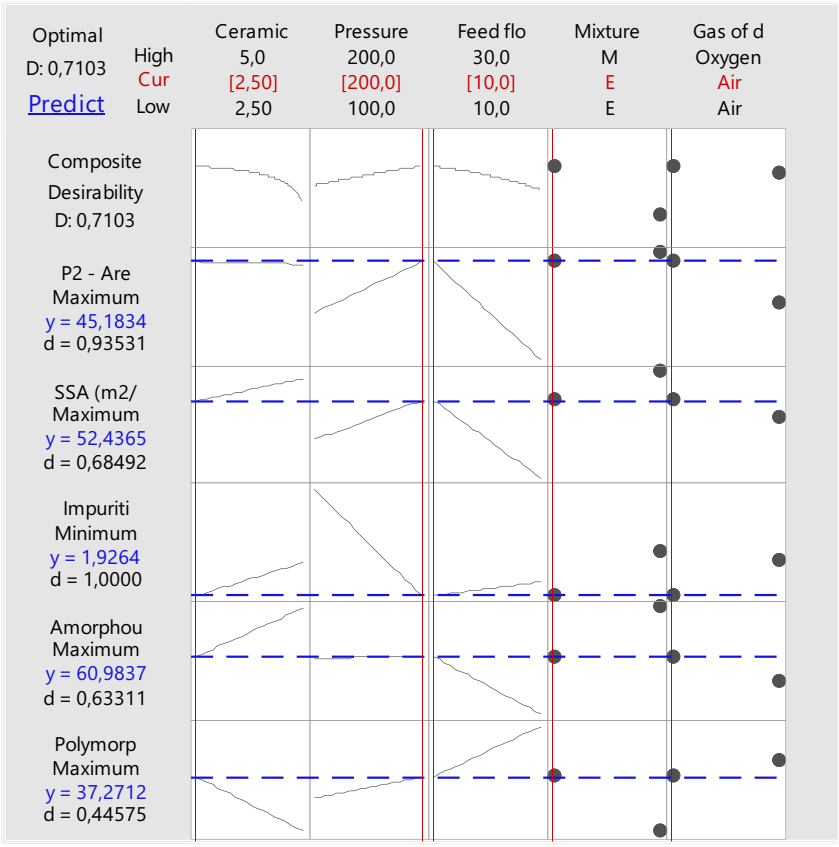

Fig. 15. Optimization plot of the variables evaluated in the FSP process.

which can be associated to honeycomb morphologies of Op C—S—H formation, while some regions show the formation of granular structures or irregular shapes associated with Ip C—S—H. This result indicates that the C—S—H formed tends to produce higher amount of inner product than outer product [42,43].

The effects of the operating variables of the FSP process during the production of calcium silicates were evaluated by means of an analysis of variance (ANOVA) comparing the means of the response variables at the different factor levels. For this, the main effects plots of the mineralogical, physical and chemical responses were analyzed (Fig. 14). The residual graphs of the fractional factorial, for all the responses, were obtained, determining that the assumptions of the model are met and validating the results.

Fig. 14 - a shows the main effects of the factors on the formation of belite polymorphs. The graph shows that the dispersion pressure, feed flow and dispersion gas factors have positive slopes, indicating that higher values of the variables favor the formation of higher amounts of belite polymorphs. In contrast, ceramic loading and solvent mixture show negative slopes, indicating that lower values favor a better response. However, the steepest slope of main effects is observed for feed rate, indicating that it is the most important variable for this response. Similarly, Fig. 14 - b shows the plot of the main effects for the amorphous fraction in the samples. It is shown that the ceramic load, the dispersion pressure and the solvent mixture do not have a significant effect, considering that the line is almost parallel to the x-axis. On the other hand, the feed flow presents a notable negative slope, which indicates that lower feed values favor the formation of amorphous material, which could be related to an easier evaporation of the droplets that favors the conversion mechanism of gas to particles.

The main effects plot for specific surface area (Fig. 14 - c) indicates that low feed rates and high dispersing gas pressure favor the formation of smaller particles. As explained above, this phenomenon may be related to the formation of smaller droplets during aerosol formation, which allows a better evaporation process during the first stage of the reaction. While the responses for the cumulative heat flow of the second peak (Fig. 14 - d) show that the steepest slope is observed for the feed flow rate, showing the main importance of these synthesis conditions. The slope for the ceramic load, the feed rate and the dispersion gas have negative values, indicating that the low level of these factors favors a higher energy release during the hydration reaction. On the other hand, the dispersion gas pressure has a positive slope, which indicates that high values favor the release of energy. These main effects present the same behavior as the main effects of the specific surface, which was expected considering that the reactivity is directly related to the contact surface of the samples with the water.

The optimal configuration of the factorial experimental design was calculated using the Response optimizer of Minitab® (Fig. 15). This graph shows how the variables were affected by the predicted responses, being composed by six columns and seven rows. The first column gives the desirability of the responses, while the columns 2 to 6 shows the response values at each level of each factor. Otherwise, the first row shows the desirability of the model and the follow rows, the optimal values for each factor (red color values).

The composite desirability of the design was of 0.7103 which indicates a good solution of the process, considering that the maximun value of these parameter is 1. This desirability is obtain when the factors take the red values show in the first column of the graph, corresponding to ceramic loading = 2.5 %, pressure of dispersion gas = 200 kPa, feed flow rate = 10 mL/min, mixture of solvents = ethanol/water, and gas of dispersion = air. The responses chosen for optimization were the percentage of the phases(polymorphs of belite, amorphous and secondary phases), the specific surface area and area of the second peak during the hydration reaction. All the responses were maximize, except the secondary phases which were minimize. The area of the first peak was not

consider due the factor in the design were not statistically significant in this response.

The first row on the right shows the predicted values for all responses. The most important answer in terms of cementitious applications is the reactivity of the samples, so the main objective was to optimize this value. The predicted value for the area of the second peak was 45.1834, with an individual desirability of 0.9353. As observed in the main effect graphs, the most important variable in the process is the feed rate, which is directly related to the size of the droplet in the aerosol, and therefore, with the efficiency of evaporation at the beginning of the reaction process.

Row 4 shows that as the feed rate decreases, all responses are maximized except for belite polymorphs and secondary phases. Regarding the secondary phases, it is a favorable result, because the design objective is to minimize the amount of non-reactive/undesirable compounds. Otherwise, regarding belite polymorphs, the results suggest that this is not the most important crystalline phase to obtain higher reactivities, since the amount of amorphous materials seems to be the most influential variable. This result suggests that the use of lower feed rates could favor the formation of most of the reactive materials, but will require longer reaction times, which implies a higher energy consumption.

The pressure of the dispersion gas was another parameter with a strong influence on the responses of the process. As shown in row 3 of the graph, high pressure values favor the maximization of all responses, while the production of secondary phases is minimized. During the process, high values of this variable promote greater disintegration of the liquid jet, allowing the formation of smaller droplets. In addition, high dispersion pressures give the particles greater kinetic energy, reducing residence times in high-temperature zones, preventing crystallization of powders and the growth process by sintering.

Regarding to the categorical response, gas of dispersion (row 6), it is interesting to see that the best results are obtained by using air, which provides lower enthalpy to the reaction, by the dissolution of the flame. This result could be linked to the type of gases used during the combustion, because the acetylene is one of the most powerful fuel gases. On the other hand, the even when the enthalpy of vaporization of the mixture of solvents, (row 5), is very close, it seems to have an important effect on the process, which could be associated to the affinity of the precursors in the solvents. Under the optimal conditions of synthesis show in the Figure, but changing the mixture of solvents, the SSA (59.11 m^2/g), area of the second peak (46.8 mJ/g) and production of amorphous material are favored (77.7 %), however, the amount of secondary phases in the system increase to values close to 6 %, which could have a bigger impact in the quality of the product. On the other hand, the minimum value of the secondary phases is the 1.92 %, by using a ceramic loading of 2.5 %. Similarly, an increase of this factor to 5 %, represents an increase of the secondary phases to 4.57 % (138 % of increment), which could be undesirable, however, the increment of these factor substantially decreases the reaction time.

Finally, it was observed that the samples with hydraulic behavior show that the synthesis conditions of the process have a strong influence on hydration. The synthesis conditions hardly influence the first hydration peak of the samples. However, the second peak of hydration shows important differences. The hydraulic behavior of these samples is very interesting, considering that in cement the belite phase has slow degree of reactivity having only significant effect after 10 days [39]. While the calorimetry curves of these samples reveal the formation of the second peak of hydration after 30 min of contact with water, indicating that enough calcium and silicon species in the solution are available to start the nucleation and growth of C—S—H species, without the observation of the induction period. Then, the belite compounds produced by FSP shown an improvement in the hydraulicity of the belite phases, since the complete hydration reaction is achieved in less than 24 h.

The samples with higher cumulative heat of hydration were $10M_{2\%}$-A_{200} and its replication, which correspond to the samples with higher SSA and higher amount of amorphous material. These samples do not have the dormant period after the dissolution of the ions in the first stage, resulting in an immediately formation of C—S—H, which can be explained by the high degree of surface in contact with water to create C—S—H nucleus, which leads to overcome the critical amount of C—S—H before the acceleration of the phase formation [39]. The results obtained with this research open up the possibility of using a continuous method for the formation of cementing phases with interesting study properties. However, it is necessary to carry out further studies on the energy efficiency of the process, costs, the release of gases and the environmental impact of the process in order to project it as a potentially applicable method in the cement industry.

4. Conclusions

The synthesis process shows the successful formation of calcium silicate phases by flame spray pyrolysis, with the presence of calcium compounds as secondary phases. The results suggest that the process has a good reproducibility of the experiments, with a remarkable importance of the process parameters over the final properties of the samples, considering that changes in these conditions affect the phase compositions and the reactivity degree of the samples. Therefore, the samples obtained can be divided in the two groups, samples with hydraulic behavior and delayed-hydraulic behavior.

The samples with lower amount of calcium carbonate were made with oxygen as dispersion air at 200 kPa (term O_{200}). The high dispersion pressure promotes the disintegration of the jet of solution to form smaller droplets, but also, this pressure gives higher kinetic energy to the particles, decreasing their time in high temperature zones, where sintering and crystallization processes take place. In addition, the use of oxygen as dispersion gas gives high energy to the flame, which favor the evaporation of the droplets in the flame. Therefore, the use of water in the starting solution lost importance when the reaction zone provides high energy levels to form a homogeneous gas phase which will react, resulting in the formation of nanoparticles with less amount of calcium oxide. Consequently, even when all the synthesis starts from the same staring solution, the variations in the process parameters, affect conditions as the time in high temperature zones and the evaporation velocity by changing the size of the drops, giving to each sample particular characteristics.

The samples with hydraulic behavior have in common the high quantity of amorphous material and the high specific surface area. In general, the number of polymorphs of belite in the samples did not suggest a strong influence on the reactivity degree of the samples, at early ages. On the other hand, the samples with higher number of secondary phases were the samples with non-hydraulic behaviors, as it could be expected.

It is possible to conclude that the best combination of process conditions to obtain hydraulic materials is acquired when the ceramic loading, pressure of dispersion gas and feed flow rate are favoring the formation of small particles. The samples obtained under these conditions, $10M_{2\%}$-A_{200} and its replication $10M_{2\%}$-A_{200}R, presented the higher reactivity. Regarding to the other conditions, when at least half of the variables plus one favor the formation of small particles, reactive samples are obtained.

CRediT authorship contribution statement

Natalia Betancur-Granados: Investigation, Formal analysis, Funding acquisition, Writing & Editing - Original Draft.

Herbert Pöllmann: Resources, Supervision.

Jorge I. Tobón: Conceptualization, Supervision, Resources, Review & Editing.

Oscar Jaime Restrepo-Baena: Methodology, Resources, Supervision, Review & Editing.

Declaration of competing interest

The authors declare that they have no known competing financial interests or personal relationships that could have appeared to influence the work reported in this paper.

Data availability

Data will be made available on request.

Acknowledgments

This work was supported by the Departamento Administrativo de Ciencia, Tecnología e Innovación (COLCIENCIAS) call 647 of 2014, Corporación Universitaria Minuto de Dios – UNIMINUTO – Project CB22-05, I2 – Innovación e Ingenería Group at UNIMINUTO, Cement and Construction Materials Research Group at the Universidad Nacional de Colombia and Mineralogy Group of the Institute of Geosciences and Geography at the Martin-Luther Universität-Germany.

In memory of Professor Herbert Pöllmann, who supported and contributed from his knowledge in cement to the development of this research.

References

[1] M.A. Alhaleeb, N.E. Machin, A simple method to set the spray properties for flame spray pyrolysis production of nanoparticles, Heliyon 6 (9) (2020), e04840, https://doi.org/10.1016/j.heliyon.2020.e04840.
[2] X. Li, A. Ouzia, K. Scrivener, Laboratory synthesis of C3S on the kilogram scale, Cem. Concr. Res. 108 (April) (2018) 201–207, https://doi.org/10.1016/j.cemconres.2018.03.019.
[3] N. Betancur-Granados, Synthesis of calcium silicates by flame spray pyrolysis [Internet], Universidad Nacional de Colombia. Universidad Nacional de Colombia, 2019, https://doi.org/10.1016/j.surfcoat.2019.125084.
[4] Z. Gou, J. Chang, Synthesis and in vitro bioactivity of dicalcium silicate powders, J. Eur. Ceram. Soc. 24 (1) (2004) 93–99.
[5] W. Booncharoen, A. Jaroenworaluck, R. Stevens, A synthesis route to nanoparticle dicalcium silicate for biomaterials research, J. Biomed. Mater. Res. Part B Appl. Biomater. 99 (2) (2011) 230–238.
[6] N. Betancur-Granados, J.C. Restrepo, J.I. Tobón, O.J. Restrepo-Baena, Dicalcium silicate (2CaO·SiO2) synthesized through flame spray pyrolysis and solution combustion synthesis methods, Ceram. Int. 45 (7) (2019) 9589–9595, https://doi.org/10.1016/j.ceramint.2018.10.073.
[7] A. Wesselsky, O.M. Jensen, Synthesis of pure Portland cement phases, Cem. Concr. Res. 39 (11) (2009) 973–980.
[8] J. Claverie, Q. Wang, S. Kamali-Bernard, F. Bernard, Assessment of the reactivity and hydration of Portland cement clinker phases from atomistic simulation: a critical review, Cem. Concr. Res. 154 (April) (2022) 2021.
[9] A. Cuesta, A. Ayuela, M.A.G. Aranda, Belite cements and their activation, Cem. Concr Res. 140 (November 2020) (2021) 106319, https://doi.org/10.1016/j.cemconres.2020.106319.
[10] O. Corona, A. Teixeira, A. Balza, Cementos Belíticos: alternativa ambiental e industrial, Investigatio (10) (2018) 10–17.
[11] K.D. Grevel, F. Bellmann, J. Majzlan, E. Dachs, A. Benisek, H.M. Ludwig, Thermodynamic data of belite polymorphs, Cem. Concr. Res. 152 (September 2021) (2022) 106621, https://doi.org/10.1016/j.cemconres.2021.106621.
[12] N. Betancur-Granados, J.I. Tobón, O.J. Restrepo-Baena, Alternative production processes of calcium silicate phases of Portland alternative production processes of calcium silicate phases of Portland cement: a review, Civ. Eng. Res. J. 5 (3) (2018) 1–6.
[13] H. Chen, H.K. Mulmudi, A. Tricoli, Flame spray pyrolysis for the one-step fabrication of transition metal oxide films: recent progress in electrochemical and photoelectrochemical water splitting, Chinese Chem Lett. 31 (3) (2020) 601–604, https://doi.org/10.1016/j.cclet.2019.05.016.
[14] N.H. Paulson, J.A. Libera, M. Stan, Flame spray pyrolysis optimization via statistics and machine learning, Mater. Des. 196 (2020) 108972, https://doi.org/10.1016/j.matdes.2020.108972.
[15] N. Betancur-Granados, J.E. Molina, H. Pöllmann, J.I. Tobón, O.J. Restrepo-Baena, Influence of metallic precursors in the mineralogy and reactivity of belite cement clinkers obtained by flame spray pyrolysis, Mater Today Commun. 26 (November 2020) (2021) 101917, https://doi.org/10.1016/j.mtcomm.2020.101917.
[16] A.H. Lefebvre, Airblast atomization, Prog. Energy Combust. Sci. 6 (1980) 233–261.
[17] S. Nukiyama, Y. Tanasawa, Experiments on the Atomization of Liquids in an Air Stream, 1950.
[18] Victor ®, Cutting, Heating and Welding Guide. Set-up and Safe Operating Procedures OXY-FUEL EQUIPMENT, 2009.
[19] A.G. De La Torre, S. Bruque, M.A.G. Aranda, Rietveld quantitative amorphous content analysis, J. Appl. Crystallogr. 34 (2) (2001) 196–202.
[20] D. Londono-Zuluaga, J.I. Tobón, M.A.G. Aranda, I. Santacruz, A.G. De la Torre, Clinkering and hydration of belite-alite-yeélimite cement, Cem. Concr. Compos. 80 (2017) 333–341.
[21] L. Fernández-Carrasco, D. Torrens-Martín, L.M. Morales, Sagrario Martínez-Ramírez, Infrared spectroscopy in the analysis of building and construction materials, Infrared Spectrosc – Mater Sci Eng 370 (2012) 369–382. Technol Technol.
[22] F. Matossi, Vibration frequencies and binding forces in some silicate groups, J. Chem. Phys. 17 (8) (1949) 679–685.
[23] M.J. Varas, M.A. De Buergo, R. Fort, Natural cement as the precursor of Portland cement: methodology for its identification, Cem. Concr. Res. 35 (11) (2005) 2055–2065.
[24] C. Shi, A.F. Jiménez, A. Palomo, New cements for the 21st century: the pursuit of an alternative to Portland cement, Cem. Concr. Res. 41 (7) (2011) 750–763.
[25] K. Garbev, B. Gasharova, P. Stemmermann, A modular concept of crystal structure applied to the thermal transformation of ??-C2 SH, J. Am. Ceram. Soc. 97 (7) (2014) 2286–2297.
[26] K. Garbev, G. Beuchle, U. Schweike, D. Merz, O. Dregert, P. Stemmermann, Preparation of a novel cementitious material from hydrothermally synthesized C-S-H phases, J. Am. Ceram. Soc. 97 (7) (2014) 2298–2307.
[27] K. Garbev, B. Gasharova, G. Beuchle, S. Kreisz, P. Stemmermann, First observation of α-Ca2[SiO3(OH)](OH)-Ca6[Si2O7][SiO4](OH)2 phase transformation upon thermal treatment in air, J. Am. Ceram. Soc. 91 (1) (2007) 263–271.
[28] F. Basquiroto de Souza, C. Zheng, S. Chen, Y. Liu, K. Sagoe-Crentsil, W. Duan, Near-field infrared microscopy: A novel analytic mapping technique to nanocharacterize calcium silicate-based cement materials, Cem Concr Res. 147 (November 2020) (2021) 106525, https://doi.org/10.1016/j.cemconres.2021.106525.
[29] A. Meiszterics, L. Rosta, H. Peterlik, J. Rohonczy, S. Kubuki, P. Henits, et al., Structural characterization of gel-derived calcium silicate systems, J. Phys. Chem. 114 (2010), 10403–11.
[30] A. Fernández-Jiménez, F. Puertas, Effect of activator mix on the hydration and strength behaviour of alkali-activated slag cements, Adv. Cem. Res. 15 (3) (2003) 129–136.
[31] Y. Yin, J. Yin, W. Zhang, H. Tian, Z. Hu, M. Ruan, et al., FT-IR and micro-raman spectroscopic characterization of minerals in high-calcium coal ashes, J. Energy Inst. 91 (3) (2018) 389–396.
[32] A.G. Xyla, G. Koutsoukos, Qantitative analysis of calcium carbonate polymorphs by infrared spectroscopy, J.Chem.Soc.Faraday Trans. 85 (10) (1989) 3165–3172.
[33] D. Chakrabarty, S.I. Kuriyavar, R. Vetrivel, S.G. Hegde, S. Mahapatra, A. V. Ramaswamy, Insights into the formation of hydroxyl ions in calcium carbonate: temperature dependent FTIR and molecular modelling studies, J. Mater. Chem. 10 (8) (2002) 1835–1840.
[34] J.P. Cain, P.L. Gassman, H. Wang, A. Laskin, Micro-FTIR study of soot chemical composition - evidence of aliphatic hydrocarbons on nascent soot surfaces, Phys. Chem. Chem. Phys. 12 (20) (2010) 5206–5218.
[35] J. Björnström, A. Martinelli, A. Matic, L. Börjesson, I. Panas, Accelerating effects of colloidal nano-silica for beneficial calcium-silicate-hydrate formation in cement, Chem. Phys. Lett. 392 (1–3) (2004) 242–248.
[36] A. Guerrero, S. Goñi, I. Campillo, A. Moragues, Belite cement clinker from coal fly ash of high ca content. Optimization of synthesis parameters, Environ. Sci. Technol. 38 (11) (2004) 3209–3213.
[37] H. Schulz, L. Mädler, S.E. Pratsinis, P. Burtscher, N. Moszner, Transparent nanocomposites of radiopaque, flame-made Ta2O5/SiO2 particles in an acrylic matrix, Adv. Funct. Mater. 15 (5) (2005) 830–837, https://doi.org/10.1002/adfm.200400234.
[38] C. Qi, H. Manzano, D. Spagnoli, Q. Chen, A. Fourie, Initial hydration process of calcium silicates in Portland cement: a comprehensive comparison from molecular dynamics simulations, Cem. Concr. Res. 149 (August) (2021), 106576, https://doi.org/10.1016/j.cemconres.2021.106576.
[39] K.L. Scrivener, P. Juilland, P.J.M. Monteiro, Advances in understanding hydration of Portland cement, Cem. Concr. Res. 78 (JUNE) (2015) 38–56.
[40] H.F.W. Taylor, Cement chemistry 2, Academic press, 1997, pp. 123–128.
[41] F. Wang, X. Kong, L. Jiang, D. Wang, The acceleration mechanism of nano-C-S-H particles on OPC hydration, Constr. Build. Mater. 249 (2020) 118734, https://doi.org/10.1016/j.conbuildmat.2020.118734.
[42] P. Paradiso, R.L. Santos, R.B. Horta, Lopes JNC, P.J. Ferreira, R. Colaço, Formation of nanocrystalline tobermorite in calcium silicate binders with low C/S ratio, Acta Mater. 152 (2018) 7–15.
[43] W. Shen, W. Zhang, J. Wang, C. Han, B. Zhang, J. Li, et al., The microstructure formation of C-S-H in the HPC paste from nano-scale feature, J. Sustain. Cem Mater. 8 (4) (2019) 199–213, https://doi.org/10.1080/21650373.2018.1564397.